# Amphisome biogenesis couples synaptic autophagy to local protein synthesis

Maria Andres-Alonso[1,2#], Catrin Schweizer[1,2#], Carolina Montenegro-Venegas[2,3], Rabia Turacak[2], Katarzyna M. Grochowska[4,5], Rabia Bice[1], Lisa Mahnke[1], Anna Karpova[1,7], Antonio Virgilio Failla[6], Eckart D. Gundelfinger[2,3,7], Michael R. Kreutz[1,2,7,8*+]

[1]Leibniz Group 'Dendritic Organelles and Synaptic Function', Center for Molecular Neurobiology Hamburg (ZMNH), University Medical Center Hamburg-Eppendorf, 20251 Hamburg, Germany

[2]Research Group 'Neuroplasticity', Leibniz Institute for Neurobiology, 39118 Magdeburg, Germany

[3]Institute for Pharmacology and Toxicology, Otto-von-Guericke University, 39120 Magdeburg, Germany

[4]Research Group 'Synaptic Proteostasis', Institute for Synaptic Neuroscience, Center for Molecular Neurobiology Hamburg (ZMNH), University Medical Center Hamburg-Eppendorf, 20251 Hamburg, Germany

[5]Institute of Cognitive Neurology and Dementia Research (IKDN), Otto-von-Guericke University, 39118 Magdeburg, Germany

[6]Microscopy Imaging Facility, University Medical Center Hamburg-Eppendorf, 20251 Hamburg, Germany

[7]Center for Behavioral Brain Sciences (CBBS), Magdeburg 39120, Germany

[8]German Center for Neurodegenerative Diseases (DZNE), Magdeburg, Germany

**Running title:**

[#]Equal contribution

*Correspondence should be addressed to MRK (michael.kreutz@lin-magdeburg.de)

[+]Lead contact

**Summary**

Amphisomes are hybrid organelles that result from fusion of late endosomes with autophagosomes. Here, we report that amphisomes containing BDNF/TrkB and capable of signaling are formed at presynaptic boutons following high-frequency stimulation. Activity dependent bulk-endocytosis serves as a membrane source and autophagy initiation is induced by the energy-sensing enzyme AMPK. Intense neuronal transmission not only induces high membrane exchange and metabolic demands, but it also causes the remodeling of presynaptic molecular composition. We show that formation of BDNF/TrkB signaling amphisomes contribute to the fast turnover of key presynaptic proteins that constitute the synaptic vesicle cluster. Following sustained synaptic activity newly-formed amphisomes enable their degradation as cargo on the one hand and their replenishment by translation of mRNA localized at synaptic boutons on the other. We propose that activity-induced synaptic autophagy to a large degree represents amphisome formation that in turn is required to replace cytomatrix proteins at presynaptic sites.

**Keywords:** Autophagy, synapse, signaling amphisomes, AMPK, bouton, synaptic vesicle cluster

## Introduction

Neurons are postmitotic cells with long processes and a large number of synaptic contacts. The extreme length and small caliber of axons pose significant challenges for proteostasis in presynaptic boutons. Very little is known how these challenges are met in terms of protein replenishment as well as degradation. The presence of mRNA and ribosomes and compelling evidence for local protein translation points to activity-dependent synaptic mechanisms that govern local replacement of proteins at boutons[1-3]. At present it is unclear, which mechanisms govern this replacement and how degradation of individual proteins is linked to their local synthesis.

The presynapse contains densely packed protein scaffolds that are involved in synaptic transmission[4-8]. Liquid-liquid phase separation-mediated organization of presynaptic compartments in the synaptic vesicle cluster (SVC) is instrumental for the localization and short-distance trafficking of synaptic vesicles (SV)[9,10]. Biomolecular condensates at the presynapse consist of highly abundant protein components including synapsin, Tau and those of the cytomatrix of the active zone (CAZ). Surprisingly little is known on how the cytoskeletal/cytomatrix proteins of the SVC are targeted to degradation at boutons.

Macroautophagy (hereafter referred to as autophagy) has been shown to be one major degradation route, tailored to the degradation of large protein complexes, toxic aggregates, and entire organelles[11]. Unlike in non-neuronal cells, autophagy in neurons appears to be highly compartmentalized. Basal autophagosome formation occurs most prominently in axons from where they are retrogradely transported to the soma where most degradative lysosomes are located[11-14]. Phagophore formation in axons under basal conditions crucially involves the endoplasmic reticulum (ER) and ER membrane[15], while other membrane sources have also been discussed and it is likely that synapse-specific adaptations of phagophore formation exist that might be regulated by synaptic activity[11,16]. The knowledge about functions and mechanisms of synaptic autophagy, however, is currently sparse.

We here show that activity-induced synaptic autophagy crucially involves the formation of amphisomes. Biogenesis of amphisomes depends upon bulk endocytosis and the recruitment as well as activation of key autophagy proteins like ULK1 induced by the energy-consumption sensing enzyme 5'-AMP-activated protein kinase (AMPK)[17-19]. Signaling of high-energy demand via AMPK during sustained synaptic vesicle release and synaptic membrane retrieval converge to generate

amphisomes that engulf key cytomatrix proteins of the SVC. Autophagic vesicles at boutons contain BDNF and active TrkB-receptors; they associate with ribosomes and induce local protein synthesis of components of the SVC and the CAZ.

## Results

Amphisome biogenesis is coupled to synaptic activity

In previous work, we and others found that amphisomes in neurons serve signaling functions by incorporating active TrkB receptors and allowing local TrkB signaling at presynaptic boutons during their retrograde transport, which ultimately enhances neurotransmission[20,21]. Recent work indicates that in developing neurons lacking mature synapses TrkB predominantly traffics in endosomes[22,23]. We therefore reasoned that biogenesis of TrkB-signaling amphisomes might be linked to synaptic function in mature neurons and that processes linked to neurotransmission might underlie their biogenesis in an activity-dependent manner. To test this hypothesis, we first assessed the presence of TrkB-containing amphisomes in axons from younger rat hippocampal neurons (DIV 5 and DIV 7) before or during early synaptogenesis in comparison to differentiated neurons (DIV 14-15) harboring several thousand functional synaptic contacts (Fig S1A-B). We indeed found in triple-labeling immunofluorescence experiments that phosphorylated TrkB (pTrkB) extensively co-localized with LC3-positive vesicles in axons immunopositive for Tau at DIV 14 (Fig 1A-B, Fig S1C). However, we did not observe co-localization at DIV5 (Fig 1A-B, Fig S1C) and at DIV7 we detected a slight but non-significant increase in LC3 vesicles positive for pTrkB (Fig S1C). The density of LC3-positive vesicles was significantly increased in neurons at DIV14 in comparison to DIV5 (Fig 1C) and, in differentiated neurons >one third of autophagy vesicles was positive for activated TrkB receptors (Fig 1D). Conversely, >40% of total detected active receptors colocalized with LC3 in mature neurons (Fig 1E). We next visualized internalized BDNF by taking advantage of BDNF coupled to qDots655 (Fig 1F). BDNF-qDot655 was added to the growing medium and the use of a non-cell-permeable fluorescence quencher allowed us to distinguish internalized qDots, which remained fluorescent, from extracellular ones whose fluorescence was quenched. Importantly, detected qDots were consistently positive for pTrkB indicating that they serve as a good tool to label signaling BDNF/TrkB complexes (Fig 1G). Using this approach, we confirmed that BDNF/TrkB complexes prominently localize to LC3-positive autophagosomes at DIV14, but not at DIV5 when we found no colocalization (Fig 1H-J; S1D-F). Thus, our results indicate that TrkB-amphisomes are found exclusively in functionally mature neurons and that TrkB localizes predominantly in signaling endosomes in developing neurons as previously described[22,23].

In light of these findings, we next asked whether synaptic activity has impact on amphisome biogenesis. To address this question, we established a protocol to electrically stimulate neurons using two electrodes placed on the coverslips with living neurons. We chose a high-frequency stimulation (HFS) protocol (900AP,10Hz) that drives the fusion of the total recycling pool of synaptic vesicles and maximizes presynaptic membrane dynamics[24,25] and we used cells electrically silenced with TTX as a control group. In comparison to silenced cultures, we observed an increased number of axonal LC3 puncta 30 min following HFS in axons at DIV15 (Fig 1K-L), suggesting that this protocol might induce robust synaptic autophagy. As outlined above in mature neurons we observed a higher amphisome number as evidenced by the overlap of LC3/pTrkB immunolabel (Fig 1M-N) than in young neurons largely devoid of boutons. In mature neurons at DIV15 HFS further increased this number while silencing of cultures with TTX had the opposite effect (Fig 1M-N). Collectively, these data suggest that the biogenesis of amphisomes is tightly linked to synaptic activity.

Autophagy and the endolysomal pathway are segregated in axons

Mature lysosomes are apparently present in axons of mature neurons[26]. Previous work suggests that amphisomes retain their signaling capacity during retrograde transport to the soma[3,20,21] which requires that amphisomes evade fusion with axonal lysosomes. To test this, we assessed the co-staining of amphisomes with lysosomal markers. We indeed found very little co-localization with the lysosomal membrane marker LAMP2A (Fig 1O-R) and the lysosomal enzyme Cathepsin D (Fig 1S-V). Moreover, no increase in lysosomal membranes was apparent in axonal amphisomes following HFS (Fig 1Q,V), and the number of autolysosomes detected by LC3 vesicles positive for LAMP2A or Cathepsin D in response to enhanced synaptic activity remained unchanged (Fig 1R,U). Thus, the autophagy and endolysosomal pathway appear to remain segregated in axons irrespective of synaptic activity.

Phagophore formation is initiated at active presynaptic boutons

In *Drosophila* neuromuscular junctions autophagosome formation has been observed at active boutons[27], however, the evidence for activity-dependent autophagy induction at presynaptic sites in mammalian neurons is sparse[11]. We reasoned that this might reflect the low abundance of autophagy-related proteins in the synaptic proteome[28] and the transient nature of activity-dependent autophagy formation at

boutons. To address these issues, we employed a novel monoclonal antibody that specifically detects phosphorylated autophagy related 16 like 1 (ATG16L1;[29]). ULK1 kinase directly phosphorylates and activates ATG16L1[30], which as part of the autophagy-related ATG12-ATG5/ATG16 complex is responsible for targeting ATG5/ATG12 to membranes of nascent autophagosomes for LC3 (ATG8) lipidation and autophagosome formation [31]. The ATG16L1/ATG5-ATG12 complex dissociates from the phagophore membrane before or around the time of autophagosome closure[31,32]. Thus, pATG16L1 immunofluorescence level provides a reliable measurement of autophagy rates and directly reflects autophagic vesicle formation. With this tool at hand, we next looked at the spatio-temporal dynamics of activity-dependent autophagy formation at boutons. We found a transient up-regulation of presynaptic pATG16L1 immunofluorescence in response to HFS at 15 minutes (Fig 2A-B). Pharmacological inhibition of ULK1/2 with SBI-0206965 prevented HFS-induced ATG16L1 phosphorylation (Fig 2B). Super-resolution imaging using STED microscopy revealed that phosphorylated ATG16L1 is found in very close association to the presynaptic scaffolding protein Bassoon (Fig 2C) and not detectable in postsynaptic dendritic spines (Fig 2D). Accordingly, no changes in pATG16L1 fluorescence were found at postsynaptic sites labeled by Shank3 (Fig S2A-B), altogether indicating that phagophore formation following HFS is restricted to presynapses. Finally, we observed that pATG16L1 immunofluorescence intensity was clearly correlated with neurotransmitter release as revealed by a synaptotagmin-uptake assay[33], suggesting a tight link to synaptic activity (Fig S2C-E).

<u>Core components of autophagy-machinery are recruited to presynaptic boutons in response to HFS</u>

A substantial increase in the number of LC3-positive vesicles, likely representing mature autophagosomes in axons, is detected about 30 min following HFS (Fig 1K-L) begging the question why there is a certain delay in phagosome maturation. We next assessed other key components of the autophagy machinery are recruited directly to boutons after stimulation of primary cultures. Within 15 minutes immunoreactivity for WIPI1/2 proteins that are required in mediating the PI3P signal at the onset of autophagy[31] was enhanced at boutons (Fig 2E-F) where it was found tightly associated to pATG16L1 in STED microscopy (Fig 2G). Similarly, the autophagy receptor p62 (Fig 2H-I), ULK1 (Fig 2J-K) and the lipid scramblase ATG9 (Fig S2F-H) were increased as compared to neurons silenced with TTX. This suggests that

autophagy proteins are recruited rapidly, i.e. within minutes, to presynaptic boutons and phagophore formation my start very close to the active zone defined by the presence of the CAZ protein Bassoon (Fig 2G).

Induction of synaptic autophagy drives the biogenesis of amphisomes

A closer inspection of phagophore formation then revealed that the vast majority of autophagic vesicles formed at boutons in an activity-dependent manner share identifiable features of signaling amphisomes. In stimulated neurons, a much higher fraction of axonal LC3-positive vesicles contain BDNF-QD-655 (Fig 2L-M) as well as active pTrkB following HFS (Fig 2N-P; Fig S2I-J). When endogenous BDNF was chelated with Fc-bodies no amphisomes were detectable in neurons silenced with TTX or after HFS (Fig 2P).

LC3-associated endocytosis (LANDO) is a noncanonical function of the autophagy machinery, in which LC3 is conjugated to rab5-positive endosomes, using a portion of the canonical autophagy pathway that is independent of ULK1 activation[34]. At variance to LANDO, presynaptic amphisome biogenesis could be blocked with the ULK1-inhibitor SBI-026965 (Fig 2P-Q).

We next aimed to gather further information regarding the nature of amphisomes and employed minimal photon fluxes (MINFLUX) nanoscopy[35] to visualize amphisome ultrastructure in neurons. To this end we employed DNA-PAINT, a technique used in single-molecule localization microscopy, to detect the localization and distribution of endogenous LC3 and active TrkB receptors. When combined with MINFLUX, DNA-PAINT allows a localization precision of ~3nm, allowing the visualization of structures at the molecular scale. With this purpose, samples were immunostained using primary antibodies against LC3 and pTrkB. Primary antibodies against LC3 were immunodetected by two secondary antibodies in parallel: αms-488 which provided a fluorescent signal in confocal microscopy and it served as structural marker; and αms-MF4 which was employed for DNA-PAINT/MINFLUX acquisitions (Fig 3A). LC3-positive structures were selected based on the signal acquired in confocal microscopy. Subsequent 3D-single-molecule localizations of LC3 in these structures were obtained using DNA-PAINT/MINFLUX imaging (Fig 3A-B). A second acquisition using DNA-PAINT/MINFLUX was performed to obtain single localizations of pTrkB in the same organelles. DNA-PAINT/MINFLUX recordings were performed for several hours to enhance the number of localizations per channel, and only localizations that

had been repeatedly found in >4 scans for each channel were considered. We found LC3 being decorating structures with sizes ranging from 300-600nm, which indicates the existence of autophagy vesicles at different stages (Fig 3C; Fig S3A-C). In larger vesicles, LC3 appeared organized forming a halo of ~80nm in thickness, resembling a doughnut with an inner space empty of LC3 or pTrkB molecules (Fig 3D-E). Given that the thickness of the biological membrane lipid bilayer ranges between 5-10 nm and that the extension of antibodies is ~15nm (i.e. ~30nm for primary/secondary antibody complexes), the area occupied by LC3 in these organelles is consistent with double-membrane organelles, where LC3 is located in the inner and outer membrane and where the inner lumen contains degradative cargo (Fig 3D). Importantly, we found TrkB localized in very close proximity/adjacent to LC3, confirming previous findings[20] as well as the double-membrane nature of TrkB-signaling amphisomes indicating that amphisome biogenesis is independent of LANDO (Fig 3D). Of note, in smaller vesicles, LC3 was prominently found occupying the organelle lumen and inner LC3-free space was not visible (Fig 3C; Fig S3B-C), further supporting the presence of LC3 inside amphisomes.

Taken together, this set of experiments shows that activity-dependent phagophore formation at boutons results in the formation of predominantly signaling amphisomes and that presynaptic autophagy in hippocampal neurons is therefore likely a distinct form of macroautophagy.

Bulk endoyctosis serves as membrane donor for amphisome formation

During high intensity stimulation synaptic vesicle endocytosis triggers activity-dependent bulk endocytosis (ADBE) to increase the retrieval capacity within the nerve terminal[36]. A simple quantitative assay of ADBE uses uptake of fluorescent dextrans of high molecular weight (40kDa) as fluid phase markers[37]. We indeed found that HFS with the stimulation regime employed in this study induces bulk endocytosis of presynaptic membrane as evidenced by increased fluorescence dextran intensity at boutons (Fig S4A-B). Interestingly, we also found an increased density of dextran puncta along axons following HFS (Fig 4B) which prominently colocalized with the amphisomal markers LC3 and pTrkB (Fig 4A-C), indicating that autophagic vesicles formed following HFS contained fluorescent dextran. Similarly, VAMP4, which is selectively recruited to large bulk endosomes[38], shows increased co-localization with amphisomes identified by means of LC3/BDNF-QD (Fig 3D-F).

We next assessed whether ADBE is a requirement for amphisome biogenesis by employing a TAT-peptide with a dominant-negative effect that specifically prevents ADBE without affecting clathrin-dependent endocytosis[39,40]. The peptides used correspond to the sequence of the dynamin I phosphobox where two serine residues are replaced by alanine to bind syndapin (Fig 3G-H; TAT-AA), while the phosphomimetic substitution (TAT-EE) has no effect (Fig 3G-H)[39]. Accordingly, incubation of neurons with TAT-AA did not have an effect on dextran uptake following HFS, while TAT-EE completely prevented HFS-induced dextran uptake at boutons (Fig 3G-H). Furthermore, the inhibition of ADBE induced by TAT-EE peptide completely blocked amphisome formation in response to HFS (Fig 3I-J) suggesting an essential role of bulk endocytosis for synaptic autophagy at boutons.

Synaptic autophagy and amphisome formation occur upon increased energy demand and AMPK activation

We next addressed potential mechanisms governing amphisome formation upon enhanced synaptic activity. Two corresponding cellular signaling pathways are known to control autophagy initiation: AMPK (adenosine monophosphate-activated protein kinase) and mTOR signaling. AMPK is the primary cellular energy sensor that is activated when the ADP/ATP or AMP/ATP ratio is increased [41]. Its activation induces autophagy by 1) inhibiting the mammalian target of rapamycin (mTOR) protein kinase complex and 2) directly activating ULK1 by direct phosphorylation[17-19]. Synaptic activity imposes large energy demands that are met by local adenosine triphosphate (ATP) synthesis through glycolysis and mitochondrial oxidative phosphorylation. In fact, 55% of ATP produced in neurons is used within boutons and axon terminals[42]. Therefore, we hypothesized that AMPK activation following HFS might be responsible for autophagy activation and amphisome biogenesis. Indeed, HFS causes AMPK activation as evidenced by a FRET-based sensor whose FRET efficiency was measured at boutons that were identified by Synaptophysin tagged with RFP (Sphy-RFP) (Fig 5A-B). Live-imaging revealed a local activation of AMPK at boutons within minutes, a time course that corresponded to increasing pATG16L1 immunofluorescence at boutons shown previously (Fig 2A-B). Most important, we could block autophagy induction at synapses (Fig 5C-D), as well as amphisome formation in response to HFS with compound C (Fig 5E-F), a pharmacological inhibitor of AMPK. In this context, treatment with Compound C prevented autophagy

induction and the increase in LC3 puncta following HFS (Fig 5G) while levels of pTrk puncta were not impaired (Fig 5H). In addition, expression of a dominant-negative form of AMPK (Fig 5I) prevented the induction of autophagy at boutons by HFS (Fig 5J-K) as well as the formation of amphisomes (Fig 5L-M). Taken together, these results suggest that bulk endocytosis and local activation of AMPK converge to induce synaptic autophagy and that activity-dependent formation of autophagic vesicles results in amphisome formation (Fig 5N).

Amphisome formation is linked to local de novo protein synthesis

It is well established that local translation regulates the axonal proteome, playing an important role in neuronal wiring and axon maintenance[43,44]. RNA granules associate with late endosomes along axons and are sites of local protein synthesis[43]. Evidence has been provided that synthesis of proteins in presynaptic terminals [1] may be involved in the local remodeling of the proteome in response to synaptic input. Such a mechanism would allow a fast and specific regulation of the proteome in response to the pattern of neuronal activity[1,45-47]. Several recent studies demonstrate local translation in mouse presynaptic terminals at adult stages[1,48-51], detecting overall 1200 translated mRNAs *in vivo*[50].

ERK-dependent signaling on local protein synthesis downstream of BDNF-TrkB has been demonstrated in soma and dendrites to regulate the structure and function of synapses[1]. In functional terms, BDNF–TrkB promotes the release of mRNAs from the RNA binding proteins responsible for their trafficking. Then, these mRNAs become readily available for translation[52,53]. BDNF-TrkB signaling amphisomes sustain neurotransmission locally in an ERK-dependent manner[20] while the underlying mechanisms are largely unclear. In light of the evidence summarized above we reasoned that amphisome biogenesis might couple synaptic autophagy to local protein synthesis.

In a first set of experiments, we could indeed show, employing a puromycilation assay, that de novo protein synthesis is increased locally at presynaptic sites in response to HFS (Fig 6A-B). Interestingly, the puromycin label was associated with about 20% of axonal amphisomes, when upon enhanced presynaptic vesicle release (Fig 6C-D), and electrical stimulation also increased the number of autophagosomes that are in close proximity to ribosomes (Fig 6E-F). We next confirmed with high-resolution STORM nanoscopy the activity-dependent tight association of LC3-positive

vesicles with ribosomes (Fig 6G-H) and two-color STED microscopy revealed that a clearly co-localization co-efficient of signaling amphisomes with ribosomes, as monitored by staining for the ribosomal protein RPS3A, at boutons after HFS (Fig 6I). Using FUNCAT labeling with the non-canonical amino acid AHA, we confirmed that protein synthesis was increased at boutons when synaptic vesicle release was enhanced by HFS and that chelation of endogenous BDNF with Fc-bodies prevented this enhanced translation at boutons (Fig 6J-K). Further evidence that biogenesis of BDNF/TrkB signaling amphisomes is instrumental for de novo protein synthesis at boutons came from experiments showing that (i) suppression of bulk endocytosis by application of the TAT-EE peptide, or (ii) inactivation ULK 1 with the antagonist SBI-026965, or (iii) blocking with AMPK activation using Comp C, suppressed HFS-induced enhancement of AHA-incorporation at presynaptic sites in hippocampal primary cultures (Fig 6L-M).

In *Bsn*- and *SIPA1L2*-deficient neurons activity-dependent amphisome formation is uncoupled from local translation

We next sought to determine in two loss-of-function genetic mouse models that interfere with different aspects of synaptic autophagy and the coupling of amphisome biogenesis to local protein translation. The CAZ protein Bassoon reportedly inhibits synaptic autophagy potentially by interacting with ATG5[54]. We indeed found much higher rates of autophagosome formation at boutons of *Bsn*-/- neurons in TTX-silenced cultures (Fig 7A-B) that remained at similar levels even after HFS (Fig 7A-B). This could reflect a ceiling effect preventing induction of additional activity-dependent autophagy. We found that AHA labeling does not increase at all at boutons in Bsn-deficient neurons following HFS (Fig 7C-D).

Following induction of presynaptic plasticity, amphisomes dissociate from dynein at boutons enabling local signaling and promoting transmitter release. This stop-over requires dissociation of SIPA1L2 from the dynein adaptor snapin[20]. In consequence, although signaling amphisomes are formed in *sipa1l2*$^{-/-}$ mice, they lose their capacity for local signaling at boutons[20]. In agreement with this previous finding, local protein synthesis was not detectable in *sipa1l2*-deficient neurons following HFS (Fig 7E-F) and expression of full-length SIPA1L2 tagged with GFP in *sipa1l2*-lacking neurons rescued this effect (Fig 7E-F) Thus, despite the formation of amphisomes, local signaling and probably docking to ribosomes, which is necessary to couple

biogenesis of these hybrid organelles to activity-dependent protein synthesis at boutons, is interrupted.

BDNF-TrkB signaling amphisomes contain proteins of presynaptic nano-biomolecular condensates and drive translation of their corresponding mRNAs

Multiple biomolecular condensates coexist at the pre- and post- synapse to enable vesicle dynamics and controlled neurotransmitter release in the brain[55]. At the presynapse, Synapsin-1 as well as Tau are known to form biomolecular condensates in the synaptic vesicle cluster that control the confinement and mobility of meso- and nanoscale synaptic vesicle domains, respectively[56,57]. Components of the CAZ including Bassoon and Piccolo further coordinate the mobility and localization of recycling vesicles[55,58]. In this context, little is known about the local turnover of Synapsin, Tau and Bassoon among others despite playing a fundamental role in ensuring presynaptic structural and functional stability. Even though the presence of local mRNA in axons of all three proteins has been reported[1,59], local translation in axons has not been previously shown. Polyribosomes are scarce in axons and local translation of axonal mRNAs at boutons reportedly occurs mainly in monosomes[3]. Monosome-preferring transcripts often encoded high-abundance synaptic proteins[3] and preferentially mRNA of proteins that have a prominent presynaptic localization associate with ribosomes in axons [3]. Interestingly, very few transmembrane proteins appear in the list of translated proteins at presynaptic monosomes[3].

Building on these previous results we first wondered which degradative cargo might be incorporated into amphisomes. Mass-spectrometry based content profiling is for various reasons very difficult to achieve and outside the scope of a single manuscript. We nevertheless took a candidate approach and observed using super-resolution STED cytoskeletal components of presynaptic biomolecular condensates are prominently present within LC3-positive vesicles (Fig 8A) in axons following HFS.

We then wondered whether TrkB-containing amphisomes drive the translation of central components of biomolecular condensates. To address this question, we established a proximity ligation assay that allowed visualization of ongoing translation of specific mRNAs at boutons (see Fig 8B). A clearly increased PLA signal in response to HFS was observed, indicating enhanced activity-induced translation of Bassoon (Fig 8C-D), Synapsin-1 (Fig 8E-F) and Tau (Fig 8G-H). No AHA-labeling and PLA signal was observed for transmembrane proteins, like the early endosome

and lysosome marker LAMP1 or the cell adhesion molecule NCAM neither in TTX conditions nor after HFS (Fig 8I-J). Scavenging of endogenous BDNF with FC-bodies prevented enhanced local translation of Bassoon following HFS (Fig 8K-L), indicating the involvement of BDNF/TrkB signaling in HFS-driven protein synthesis at boutons. Direct evidence that stalling of signaling amphisomes at boutons and interaction with ribosomes are crucial for activity-dependent translation of cytoskeletal protein components of the synaptic vesicle cluster was provided by experiments with SIPA1L2-/- neurons. Gene knockout of this RapGAP resulted in a complete loss of activity-dependent de novo protein synthesis of Bsn (Fig 8M-N) and Tau at boutons (Fig 8O-P).

## Discussion

In previous work, we and others described a mechanism whereby autophagic vesicles acquire signaling functions that is based on the incorporation of TrkB receptors to autophagosomes[20,21]. Before ultimately fusing with lysosomes, autophagosomes can fuse with late endosomes (LEs) / multivesicular bodies (MVBs) to generate an intermediate / hybrid organelle - the amphisome. While this work provided first evidence for signaling amphisomes in neurons key questions remained on just how TrkB-containing amphisomes play a role in signaling at single presynaptic terminals and their link to synaptic function. The key findings of the present study indicate that i) signaling amphisome biogenesis occurs at presynaptic boutons in differentiated neurons in an activity-dependent manner, ii) synaptic autophagy in hippocampal pyramidal neurons prominently includes amphisome formation, iii) autophagic and endolysosomal pathways appear to be segregated in axons, iv) bulk endocytosis and AMPK energy sensing converge for presynaptic phagophore formation, v) signaling amphisomes contain proteins of presynaptic nano-biomolecular condensates and drive translation of their corresponding mRNAs (see Figure S5).

### Induction of autophagy at boutons results in the formation of signaling amphisomes

One key question in the study of neuronal autophagy concerns the distinction between ongoing basal autophagy and autophagy induced by synaptic input. Along these lines, it is currently unclear whether targets of autophagic degradation are altered during induced autophagy, or whether just the rate of autophagy alone changes. Cargo availability for engulfment is independent of the mechanisms of autophagy induction, but depends upon first, the relative abundance of cargo; second, the time and location of autophagosome biogenesis relative to the localization of the cargo; and third, the direct or indirect molecular interaction of cargo with early-acting components of the autophagic machinery (e.g. autophagy adaptors or receptors) during phagophore formation. To study this “contextual specificity” at boutons[11], we have used a physiologically relevant protocol for HFS that induces sustained synaptic vesicle release and bulk endocytosis[24]. Moreover, HFS induces synaptic autophagy that includes amphisome formation and that might be predominant given that membrane from bulk endosomes, likely containing TrkB, appears to contribute to the formation of autophagic vesicles. We therefore assume

that synaptic autophagosomes are different from those generated in other neuronal sub-compartments, not only in terms of content, but also in terms of function. At present we have no evidence that only certain presynaptic proteins are sorted for autophagic degradation. Content profiling will be necessary to provide a final answer whether selective or non-selective autophagy of degradative cargo is predominant at boutons. Nonetheless, the data obtained so far suggest that content of activity-induced synaptic autophagosomes is obviously distinct from bulk autophagy under basal conditions that largely resembles ER-phagy[15,60]. Evidence for separate mechanisms underlying basal and activity-regulated autophagic processes in the presynapse comes also from preliminary work on the *Drosophila* neuromuscular junction, where the regulation of activity-dependent degradation of SV components, but not of starvation-dependent autophagy, involves the vesicular membrane protein synaptogyrin[61].

Mechanistic underpinnings of amphisome biogenesis

The scarcity of autophagy-related proteins in the presynaptic proteome and the lack of compelling evidence that autophagosomes are indeed formed in an activity-dependent manner at boutons in mammalia requested a systematic analysis with higher temporal and spatial resolution. Our results suggest that the phagophore is closed and cargo loading is completed at boutons within several minutes. We assume that this time course at least in part also reflects the necessity to recruit autophagy-related proteins to the presynapse. At present, it is unclear how enhanced synaptic activity following HFS relates to recruitment of core autophagic proteins, but one possible candidate is AMPK-signaling. We found that energy-sensing by AMPK is instrumental for phagophore formation and a pressing question concerns other processes that converge at boutons to generate amphisomes. Of particular interest is here the tight linkage between autophagic and endocytic factors[62-64]. Endophilin-A for instance, which is crucially involved in retrieval of membranes following the fusion SVs with the presynaptic AZ[65-67] is also a major player in generating initiation sites for autophagy[27,68]. The lipid phosphatase Synaptojanin-1 is recruited to Endophilin-A complexes and regulates the association of the lipid-binding protein ATG18a on nascent autophagosomes[69]. The AP-2 complex is involved in endocytosis during SV recycling[70,71] and can directly interact with ATG9A[72], a lipid scramblase that is involved in early steps of phagophore formation[73]. Trafficking of ATG9 to boutons

and insertion in the presynaptic membrane is a prerequisite for autophagy initiation and progression[74]. Thus, it will be interesting to study how these molecular interactions are related to bulk endocytosis, AMPK signaling and amphisome biogenesis.

Another important question concerns the membrane source for phagophore formation and how far autophagosome formation proceeds into the presynapse. We suppose that bulk endosomes (BE) containing ATG9 and BDNF/TrkB receptors are formed upon HFS. After closure, a BE could fuse to an existing autophagosome to form a signaling amphisome. Alternatively, a BE might move closer to the ER below the bouton where ATG2 then supplies phospholipids for autophagosome formation. In this scenario, the membrane content of the BE will become part of the signaling amphisome. BE can also serve as a lipid source for an ATG9-containing carrier to grow into an autophagosome which will contribute to amphisome biogenesis.

Amphisomes control selective mRNA translation in neuronal subcellular compartments

A central finding of this study is that amphisome biogenesis connects synaptic autophagy to local protein synthesis. Our data suggest that signaling amphisomes might couple energy demand due to increased SV release to rejuvenate the presynaptic pool. Sustained vesicular release likely comes along with increased protein damage and the necessity to replace proteins. The apparent low basal content of mRNA and protein synthesis machinery in axons requires a rather local and efficient mechanism to replenish presynaptic proteins[75]. We propose that signaling amphisomes could provide an efficient means to provide input specificity. Local translation provides a source for proteins that are used as close as 1–20 µm from their site of synthesis to elicit an effect[47,75,76]. The stop-over of amphisomes at boutons requires presynaptic activity and BDNF/TrkB signaling is restricted to highly active presynapses[20] and signaling appear to highly stable organelles because the endolysosomal and autophagy pathway remain largely segregated in axons.

The mTOR pathway acts as a central regulator for metabolism by balancing protein synthesis and degradation. When mTOR is active it promotes protein synthesis while simultaneously suppressing autophagy[77]. Conversely, mTOR inhibition leads to the activation of autophagy. One might therefore ask how can the same pathway that when it is active promote protein synthesis has to be inhibited to induce autophagy

more or less at the same time? We suppose that there is a spatial segregation and that mTORC1 is absent from autophagy initiation sites at the active zone. AMPK can activate Ulk1 directly and thereby trigger autophagy induction[77,78]. Moreover, we were not able to induce autophagy in axons with rapamycin at a time scale relevant for this study (data not shown), supporting the idea that synaptic autophagy is not under control of the mTOR pathway.

A potential role of Bassoon in activity-dependent synaptic autophagy, amphisome formation and local protein synthesis

Bassoon is currently the only protein component of the CAZ that appears to regulate autophagy via an interaction with ATG5. However, apparent discrepancies exist in phenotypes of ATG5 and Bsn-deficient mice and Bassoon is crucially involved in controlling presynaptic protein turnover in multiple ways that might indirectly interfere with the study of synaptic autophagy and that might accumulate over time. Lack of Bassoon increases BDNF/TrkB levels[79,80] as well as autophagy[54,81] and proteasomal activity[82]. We found that phagophore formation as evidenced by ATG16L1 phosphorylation is prominently enhanced at boutons of Bsn-deficient cells in the presence of TTX and that HFS has no further effect on this measure. We suppose that Bassoon controls the activity-dependent pathway and that therefore no further activation of this pathway can occur upon stimulation. In other terms, the inhibition of ATG5 function by Bassoon at rest prevents elevated phagophore formation unless activity-dependent synaptic autophagy kicks-in. This, however, is a prerequisite for amphisome biogenesis in response to HFS.

Functional consequences of amphisome signaling for the integrity of the SVC and nanodomains in biomolecular condensates

Local protein translation at boutons largely occurs at monosomes and despite some ribosome heterogeneity the emerging picture that mainly highly abundant non-transmembrane synaptic proteins undergo activity-dependent de novo synthesis[3]. Our results with a candidate approach support this view. The structure and integrity of the SVC crucially depend on cytoskeletal proteins, like synapsin, tau and proteins of the CAZ. These proteins form a dense meshwork that contains RNA, they undergo liquid-liquid phase separation to generate presynaptic nanoclusters whose density and number are regulated by activity. It has been proposed that they organize the

nanoscale organization of synaptic vesicles, a process that is still poorly understood. It is tempting to speculate that signaling amphisomes replenish prominently proteins forming biomolecular condensates in a highly localized manner.

## Supplemental information

Supplemental information can be found online …

## Acknowledgments

The authors wish to thank Corinna Borutzki, Isabel Herbert and Monika Marunde for excellent technical assistance. We acknowledge the support of UMIF staff at UKE.
The authors received funding from the German Research Foundation (DFG) FOR5228 (RP06 to A.K. and M.R.K. and RP03 to E.D.G.) and ERC grant LEXSYN, Number 101161748 (K.M.G.).

## Author contributions

M.A.A. and C.S. contributed equally to this work. M.A.A., E.D.G. and M.R.K. designed the experiments. M.A.A., C.S., R.T., C.M.V., K.M.G., R.B., L.M., A.K., A.V.F. performed the experiments and analyzed the data. M.A.A. and C.S. prepared the figures. M.R.K. conceptualized the study and wrote the manuscript together with M.A.A. and E.D.G.. All authors read and commented on the manuscript.

## Declaration of interests

The authors declare no competing interest.

## References


1. Hafner, A.S., Donlin-Asp, P.G., Leitch, B., Herzog, E., and Schuman, E.M. (2019). Local protein synthesis is a ubiquitous feature of neuronal pre- and postsynaptic compartments. Science *364*. 10.1126/science.aau3644.
2. Rankovic, B., Geisterfer, Z.M., Chhabra, A., V.M., J., Seim, I., Hoffmann, C., Condric, A., Aguilar Pérez, G., Freitag, K., Nowick, K., et al. (2025). RNA promotes synapsin coacervation and modulates local translation. bioRxiv. https://doi.org/10.1101/2025.01.29.635107.
3. Biever, A., Glock, C., Tushev, G., Ciirdaeva, E., Dalmay, T., Langer, J.D., and Schuman, E.M. (2020). Monosomes actively translate synaptic mRNAs in neuronal processes. Science *367*. 10.1126/science.aay4991.
4. Ackermann, F., Waites, C.L., and Garner, C.C. (2015). Presynaptic active zones in invertebrates and vertebrates. EMBO Rep *16*, 923-938. 10.15252/embr.201540434.
5. Schoch, S., and Gundelfinger, E.D. (2006). Molecular organization of the presynaptic active zone. Cell Tissue Res *326*, 379-391. 10.1007/s00441-006-0244-y.
6. Siksou, L., Rostaing, P., Lechaire, J.P., Boudier, T., Ohtsuka, T., Fejtova, A., Kao, H.T., Greengard, P., Gundelfinger, E.D., Triller, A., and Marty, S. (2007). Three-dimensional architecture of presynaptic terminal cytomatrix. J Neurosci *27*, 6868-6877. 27/26/6868 [pii]10.1523/JNEUROSCI.1773-07.2007.
7. Sudhof, T.C. (2012). The presynaptic active zone. Neuron *75*, 11-25. 10.1016/j.neuron.2012.06.012.
8. Wilhelm, B.G., Mandad, S., Truckenbrodt, S., Krohnert, K., Schafer, C., Rammner, B., Koo, S.J., Classen, G.A., Krauss, M., Haucke, V., et al. (2014). Composition of isolated synaptic boutons reveals the amounts of vesicle trafficking proteins. Science *344*, 1023-1028. 344/6187/1023 [pii] 10.1126/science.1252884.
9. Milovanovic, D., and De Camilli, P. (2017). Synaptic Vesicle Clusters at Synapses: A Distinct Liquid Phase? Neuron *93*, 995-1002. 10.1016/j.neuron.2017.02.013.
10. Milovanovic, D., Wu, Y., Bian, X., and De Camilli, P. (2018). A liquid phase of synapsin and lipid vesicles. Science *361*, 604-607. 10.1126/science.aat5671.
11. Karpova, A., Hiesinger, P.R., Kuijpers, M., Albrecht, A., Kirstein, J., Andres-Alonso, M., Biermeier, A., Eickholt, B.J., Mikhaylova, M., Maglione, M., et al. (2025). Neuronal autophagy in the control of synapse function. Neuron *113*, 974-990. 10.1016/j.neuron.2025.01.019.
12. Andres-Alonso, M., Kreutz, M.R., and Karpova, A. (2021). Autophagy and the endolysosomal system in presynaptic function. Cell Mol Life Sci *78*, 2621-2639. 10.1007/s00018-020-03722-5.
13. Grochowska, K.M., Andres-Alonso, M., Karpova, A., and Kreutz, M.R. (2022). The needs of a synapse-How local organelles serve synaptic proteostasis. EMBO J *41*, e110057. 10.15252/embj.2021110057.
14. Stavoe, A.K.H., and Holzbaur, E.L.F. (2019). Autophagy in Neurons. Annu Rev Cell Dev Biol *35*, 477-500. 10.1146/annurev-cellbio-100818-125242.
15. Kuijpers, M., Kochlamazashvili, G., Stumpf, A., Puchkov, D., Swaminathan, A., Lucht, M.T., Krause, E., Maritzen, T., Schmitz, D., and Haucke, V. (2021). Neuronal Autophagy Regulates Presynaptic Neurotransmission by Controlling the Axonal Endoplasmic Reticulum. Neuron *109*, 299-313 e299. 10.1016/j.neuron.2020.10.005.
16. Wosnitzka, E., Gambarotto, L., and Nikoletopoulou, V. (2025). Macroautophagy at the service of synapses. Curr Opin Neurobiol *93*, 103054. 10.1016/j.conb.2025.103054.
17. Feng, Y., Chen, Y., Wu, X., Chen, J., Zhou, Q., Liu, B., Zhang, L., and Yi, C. (2024). Interplay of energy metabolism and autophagy. Autophagy *20*, 4-14. 10.1080/15548627.2023.2247300.
18. Mao, K., and Klionsky, D.J. (2011). AMPK activates autophagy by phosphorylating ULK1. Circ Res *108*, 787-788. 10.1161/RES.0b013e3182194c29.
19. Egan, D.F., Shackelford, D.B., Mihaylova, M.M., Gelino, S., Kohnz, R.A., Mair, W., Vasquez, D.S., Joshi, A., Gwinn, D.M., Taylor, R., et al. (2011). Phosphorylation of

ULK1 (hATG1) by AMP-activated protein kinase connects energy sensing to mitophagy. Science *331*, 456-461. 10.1126/science.1196371.
20. Andres-Alonso, M., Ammar, M.R., Butnaru, I., Gomes, G.M., Acuna Sanhueza, G., Raman, R., Yuanxiang, P., Borgmeyer, M., Lopez-Rojas, J., Raza, S.A., et al. (2019). SIPA1L2 controls trafficking and local signaling of TrkB-containing amphisomes at presynaptic terminals. Nat Commun *10*, 5448. 10.1038/s41467-019-13224-z.
21. Kononenko, N.L., Classen, G.A., Kuijpers, M., Puchkov, D., Maritzen, T., Tempes, A., Malik, A.R., Skalecka, A., Bera, S., Jaworski, J., and Haucke, V. (2017). Retrograde transport of TrkB-containing autophagosomes via the adaptor AP-2 mediates neuronal complexity and prevents neurodegeneration. Nat Commun *8*, 14819. 10.1038/ncomms14819.
22. Kulkarni, V.V., Stempel, M.H., Anand, A., Sidibe, D.K., and Maday, S. (2022). Retrograde Axonal Autophagy and Endocytic Pathways Are Parallel and Separate in Neurons. J Neurosci *42*, 8524-8541. 10.1523/JNEUROSCI.1292-22.2022.
23. Sidibe, D.K., Kulkarni, V.V., Dong, A., Herr, J.B., Vogel, M.C., Stempel, M.H., and Maday, S. (2022). Brain-derived neurotrophic factor stimulates the retrograde pathway for axonal autophagy. J Biol Chem *298*, 102673. 10.1016/j.jbc.2022.102673.
24. Fernandez-Alfonso, T., and Ryan, T.A. (2004). The kinetics of synaptic vesicle pool depletion at CNS synaptic terminals. Neuron *41*, 943-953. 10.1016/s0896-6273(04)00113-8.
25. Kwon, S.E., and Chapman, E.R. (2011). Synaptophysin regulates the kinetics of synaptic vesicle endocytosis in central neurons. Neuron *70*, 847-854. 10.1016/j.neuron.2011.04.001.
26. Lie, P.P.Y., Yang, D.S., Stavrides, P., Goulbourne, C.N., Zheng, P., Mohan, P.S., Cataldo, A.M., and Nixon, R.A. (2021). Post-Golgi carriers, not lysosomes, confer lysosomal properties to pre-degradative organelles in normal and dystrophic axons. Cell Rep *35*, 109034. 10.1016/j.celrep.2021.109034.
27. Soukup, S.F., Kuenen, S., Vanhauwaert, R., Manetsberger, J., Hernandez-Diaz, S., Swerts, J., Schoovaerts, N., Vilain, S., Gounko, N.V., Vints, K., et al. (2016). A LRRK2-Dependent EndophilinA Phosphoswitch Is Critical for Macroautophagy at Presynaptic Terminals. Neuron *92*, 829-844. 10.1016/j.neuron.2016.09.037.
28. Gundelfinger, E.D., Karpova, A., Pielot, R., Garner, C.C., and Kreutz, M.R. (2022). Organization of Presynaptic Autophagy-Related Processes. Front Synaptic Neurosci *14*, 829354. 10.3389/fnsyn.2022.829354.
29. Tian, W., Alsaadi, R., Guo, Z., Kalinina, A., Carrier, M., Tremblay, M.E., Lacoste, B., Lagace, D., and Russell, R.C. (2020). An antibody for analysis of autophagy induction. Nat Methods *17*, 232-239. 10.1038/s41592-019-0661-y.
30. Alsaadi, R.M., Losier, T.T., Tian, W., Jackson, A., Guo, Z., Rubinsztein, D.C., and Russell, R.C. (2019). ULK1-mediated phosphorylation of ATG16L1 promotes xenophagy, but destabilizes the ATG16L1 Crohn's mutant. EMBO Rep *20*, e46885. 10.15252/embr.201846885.
31. Dikic, I., and Elazar, Z. (2018). Mechanism and medical implications of mammalian autophagy. Nat Rev Mol Cell Biol *19*, 349-364. 10.1038/s41580-018-0003-4.
32. Hamaoui, D., and Subtil, A. (2022). ATG16L1 functions in cell homeostasis beyond autophagy. FEBS J *289*, 1779-1800. 10.1111/febs.15833.
33. Kraszewski, K., Mundigl, O., Daniell, L., Verderio, C., Matteoli, M., and De Camilli, P. (1995). Synaptic vesicle dynamics in living cultured hippocampal neurons visualized with CY3-conjugated antibodies directed against the lumenal domain of synaptotagmin. J Neurosci *15*, 4328-4342. 10.1523/JNEUROSCI.15-06-04328.1995.
34. Magne, J., and Green, D.R. (2022). LC3-associated endocytosis and the functions of Rubicon and ATG16L1. Sci Adv *8*, eabo5600. 10.1126/sciadv.abo5600.
35. Schmidt, R., Weihs, T., Wurm, C.A., Jansen, I., Rehman, J., Sahl, S.J., and Hell, S.W. (2021). MINFLUX nanometer-scale 3D imaging and microsecond-range tracking on a common fluorescence microscope. Nat Commun *12*, 1478. 10.1038/s41467-021-21652-z.

36. Clayton, E.L., and Cousin, M.A. (2009). The molecular physiology of activity-dependent bulk endocytosis of synaptic vesicles. J Neurochem *111*, 901-914. 10.1111/j.1471-4159.2009.06384.x.
37. Clayton, E.L., Evans, G.J., and Cousin, M.A. (2008). Bulk synaptic vesicle endocytosis is rapidly triggered during strong stimulation. J Neurosci *28*, 6627-6632. 10.1523/JNEUROSCI.1445-08.2008.
38. Nicholson-Fish, J.C., Kokotos, A.C., Gillingwater, T.H., Smillie, K.J., and Cousin, M.A. (2015). VAMP4 Is an Essential Cargo Molecule for Activity-Dependent Bulk Endocytosis. Neuron *88*, 973-984. 10.1016/j.neuron.2015.10.043.
39. Anggono, V., Smillie, K.J., Graham, M.E., Valova, V.A., Cousin, M.A., and Robinson, P.J. (2006). Syndapin I is the phosphorylation-regulated dynamin I partner in synaptic vesicle endocytosis. Nat Neurosci *9*, 752-760. 10.1038/nn1695.
40. Clayton, E.L., Anggono, V., Smillie, K.J., Chau, N., Robinson, P.J., and Cousin, M.A. (2009). The phospho-dependent dynamin-syndapin interaction triggers activity-dependent bulk endocytosis of synaptic vesicles. J Neurosci *29*, 7706-7717. 10.1523/JNEUROSCI.1976-09.2009.
41. Li, S., and Sheng, Z.H. (2022). Energy matters: presynaptic metabolism and the maintenance of synaptic transmission. Nat Rev Neurosci *23*, 4-22. 10.1038/s41583-021-00535-8.
42. Li, S., Xiong, G.J., Huang, N., and Sheng, Z.H. (2020). The cross-talk of energy sensing and mitochondrial anchoring sustains synaptic efficacy by maintaining presynaptic metabolism. Nat Metab *2*, 1077-1095. 10.1038/s42255-020-00289-0.
43. Cioni, J.M., Lin, J.Q., Holtermann, A.V., Koppers, M., Jakobs, M.A.H., Azizi, A., Turner-Bridger, B., Shigeoka, T., Franze, K., Harris, W.A., and Holt, C.E. (2019). Late Endosomes Act as mRNA Translation Platforms and Sustain Mitochondria in Axons. Cell *176*, 56-72 e15. 10.1016/j.cell.2018.11.030.
44. Castillo, P.E., Jung, H., Klann, E., and Riccio, A. (2023). Presynaptic Protein Synthesis in Brain Function and Disease. J Neurosci *43*, 7483-7488. 10.1523/JNEUROSCI.1454-23.2023.
45. Fonkeu, Y., Kraynyukova, N., Hafner, A.S., Kochen, L., Sartori, F., Schuman, E.M., and Tchumatchenko, T. (2019). How mRNA Localization and Protein Synthesis Sites Influence Dendritic Protein Distribution and Dynamics. Neuron *103*, 1109-1122 e1107. 10.1016/j.neuron.2019.06.022.
46. Rangaraju, V., Lauterbach, M., and Schuman, E.M. (2019). Spatially Stable Mitochondrial Compartments Fuel Local Translation during Plasticity. Cell *176*, 73-84 e15. 10.1016/j.cell.2018.12.013.
47. Rangaraju, V., tom Dieck, S., and Schuman, E.M. (2017). Local translation in neuronal compartments: how local is local? EMBO Rep *18*, 693-711. 10.15252/embr.201744045.
48. Monday, H.R., Kharod, S.C., Yoon, Y.J., Singer, R.H., and Castillo, P.E. (2022). Presynaptic FMRP and local protein synthesis support structural and functional plasticity of glutamatergic axon terminals. Neuron *110*, 2588-2606 e2586. 10.1016/j.neuron.2022.05.024.
49. Ostroff, L.E., Santini, E., Sears, R., Deane, Z., Kanadia, R.N., LeDoux, J.E., Lhakhang, T., Tsirigos, A., Heguy, A., and Klann, E. (2019). Axon TRAP reveals learning-associated alterations in cortical axonal mRNAs in the lateral amgydala. Elife *8*. 10.7554/eLife.51607.
50. Shigeoka, T., Jung, H., Jung, J., Turner-Bridger, B., Ohk, J., Lin, J.Q., Amieux, P.S., and Holt, C.E. (2016). Dynamic Axonal Translation in Developing and Mature Visual Circuits. Cell *166*, 181-192. 10.1016/j.cell.2016.05.029.
51. Younts, T.J., Monday, H.R., Dudok, B., Klein, M.E., Jordan, B.A., Katona, I., and Castillo, P.E. (2016). Presynaptic Protein Synthesis Is Required for Long-Term Plasticity of GABA Release. Neuron *92*, 479-492. 10.1016/j.neuron.2016.09.040.
52. Costa, R.O., Martins, L.F., Tahiri, E., and Duarte, C.B. (2022). Brain-derived neurotrophic factor-induced regulation of RNA metabolism in neuronal development and synaptic plasticity. Wiley Interdiscip Rev RNA *13*, e1713. 10.1002/wrna.1713.

53. Sahoo, P.K., Smith, D.S., Perrone-Bizzozero, N., and Twiss, J.L. (2018). Axonal mRNA transport and translation at a glance. J Cell Sci *131*. 10.1242/jcs.196808.
54. Okerlund, N.D., Schneider, K., Leal-Ortiz, S., Montenegro-Venegas, C., Kim, S.A., Garner, L.C., Waites, C.L., Gundelfinger, E.D., Reimer, R.J., and Garner, C.C. (2017). Bassoon Controls Presynaptic Autophagy through Atg5. Neuron *93*, 897-913 e897. 10.1016/j.neuron.2017.01.026.
55. Reshetniak, S., Bogaciu, C.A., Bonn, S., Brose, N., Cooper, B.H., D'Este, E., Fauth, M., Fernandez-Busnadiego, R., Fiosins, M., Fischer, A., et al. (2024). The synaptic vesicle cluster as a controller of pre- and postsynaptic structure and function. J Physiol. 10.1113/JP286400.
56. Hoffmann, C., Rentsch, J., Tsunoyama, T.A., Chhabra, A., Aguilar Perez, G., Chowdhury, R., Trnka, F., Korobeinikov, A.A., Shaib, A.H., Ganzella, M., et al. (2023). Synapsin condensation controls synaptic vesicle sequestering and dynamics. Nat Commun *14*, 6730. 10.1038/s41467-023-42372-6.
57. Longfield, S.F., Mollazade, M., Wallis, T.P., Gormal, R.S., Joensuu, M., Wark, J.R., van Waardenberg, A.J., Small, C., Graham, M.E., Meunier, F.A., and Martinez-Marmol, R. (2023). Tau forms synaptic nano-biomolecular condensates controlling the dynamic clustering of recycling synaptic vesicles. Nat Commun *14*, 7277. 10.1038/s41467-023-43130-4.
58. Qiu, H., Wu, X., Ma, X., Li, S., Cai, Q., Ganzella, M., Ge, L., Zhang, H., and Zhang, M. (2024). Short-distance vesicle transport via phase separation. Cell *187*, 2175-2193 e2121. 10.1016/j.cell.2024.03.003.
59. Glock, C., Biever, A., Tushev, G., Nassim-Assir, B., Kao, A., Bartnik, I., Tom Dieck, S., and Schuman, E.M. (2021). The translatome of neuronal cell bodies, dendrites, and axons. Proc Natl Acad Sci U S A *118*. 10.1073/pnas.2113929118.
60. Yperman, K., and Kuijpers, M. (2023). Neuronal endoplasmic reticulum architecture and roles in axonal physiology. Mol Cell Neurosci *125*, 103822. 10.1016/j.mcn.2023.103822.
61. Hernandez-Diaz, S., Martinez-Olondo, P., Sanchez-Mirasierra, I., Montecinos, C., Ghimire, S., and Soukup, S.-F. (2023). Synaptogyrin regulates neuronal activity dependent autophagy to degrade synaptic vesicle components and pathological Tau. bioRxiv. 10.1101/2023.07.04.547658.
62. Azarnia Tehran, D., Kuijpers, M., and Haucke, V. (2018). Presynaptic endocytic factors in autophagy and neurodegeneration. Curr Opin Neurobiol *48*, 153-159. 10.1016/j.conb.2017.12.018.
63. Soukup, S.F., and Verstreken, P. (2017). EndoA/Endophilin-A creates docking stations for autophagic proteins at synapses. Autophagy *13*, 971-972. 10.1080/15548627.2017.1286440.
64. Vijayan, V., and Verstreken, P. (2017). Autophagy in the presynaptic compartment in health and disease. J Cell Biol *216*, 1895-1906. 10.1083/jcb.201611113.
65. Boucrot, E., Ferreira, A.P., Almeida-Souza, L., Debard, S., Vallis, Y., Howard, G., Bertot, L., Sauvonnet, N., and McMahon, H.T. (2015). Endophilin marks and controls a clathrin-independent endocytic pathway. Nature *517*, 460-465. 10.1038/nature14067.
66. Milosevic, I., Giovedi, S., Lou, X., Raimondi, A., Collesi, C., Shen, H., Paradise, S., O'Toole, E., Ferguson, S., Cremona, O., and De Camilli, P. (2011). Recruitment of endophilin to clathrin-coated pit necks is required for efficient vesicle uncoating after fission. Neuron *72*, 587-601. 10.1016/j.neuron.2011.08.029.
67. Watanabe, S., Mamer, L.E., Raychaudhuri, S., Luvsanjav, D., Eisen, J., Trimbuch, T., Sohl-Kielczynski, B., Fenske, P., Milosevic, I., Rosenmund, C., and Jorgensen, E.M. (2018). Synaptojanin and Endophilin Mediate Neck Formation during Ultrafast Endocytosis. Neuron *98*, 1184-1197 e1186. 10.1016/j.neuron.2018.06.005.
68. Murdoch, J.D., Rostosky, C.M., Gowrisankaran, S., Arora, A.S., Soukup, S.F., Vidal, R., Capece, V., Freytag, S., Fischer, A., Verstreken, P., et al. (2016). Endophilin-A Deficiency Induces the Foxo3a-Fbxo32 Network in the Brain and Causes

Dysregulation of Autophagy and the Ubiquitin-Proteasome System. Cell Rep *17*, 1071-1086. 10.1016/j.celrep.2016.09.058.
69. Vanhauwaert, R., Kuenen, S., Masius, R., Bademosi, A., Manetsberger, J., Schoovaerts, N., Bounti, L., Gontcharenko, S., Swerts, J., Vilain, S., et al. (2017). The SAC1 domain in synaptojanin is required for autophagosome maturation at presynaptic terminals. EMBO J *36*, 1392-1411. 10.15252/embj.201695773.
70. Kononenko, N.L., Puchkov, D., Classen, G.A., Walter, A.M., Pechstein, A., Sawade, L., Kaempf, N., Trimbuch, T., Lorenz, D., Rosenmund, C., et al. (2014). Clathrin/AP-2 mediate synaptic vesicle reformation from endosome-like vacuoles but are not essential for membrane retrieval at central synapses. Neuron *82*, 981-988. 10.1016/j.neuron.2014.05.007.
71. McMahon, H.T., and Boucrot, E. (2011). Molecular mechanism and physiological functions of clathrin-mediated endocytosis. Nat Rev Mol Cell Biol *12*, 517-533. 10.1038/nrm3151.
72. Imai, K., Hao, F., Fujita, N., Tsuji, Y., Oe, Y., Araki, Y., Hamasaki, M., Noda, T., and Yoshimori, T. (2016). Atg9A trafficking through the recycling endosomes is required for autophagosome formation. J Cell Sci *129*, 3781-3791. 10.1242/jcs.196196.
73. Sawa-Makarska, J., Baumann, V., Coudevylle, N., von Bulow, S., Nogellova, V., Abert, C., Schuschnig, M., Graef, M., Hummer, G., and Martens, S. (2020). Reconstitution of autophagosome nucleation defines Atg9 vesicles as seeds for membrane formation. Science *369*. 10.1126/science.aaz7714.
74. Yang, S., Park, D., Manning, L., Hill, S.E., Cao, M., Xuan, Z., Gonzalez, I., Dong, Y., Clark, B., Shao, L., et al. (2022). Presynaptic autophagy is coupled to the synaptic vesicle cycle via ATG-9. Neuron. 10.1016/j.neuron.2021.12.031.
75. Cagnetta, R., Flanagan, J.G., and Sonenberg, N. (2023). Control of Selective mRNA Translation in Neuronal Subcellular Compartments in Health and Disease. J Neurosci *43*, 7247-7263. 10.1523/JNEUROSCI.2240-22.2023.
76. Bourke, A.M., Schwarz, A., and Schuman, E.M. (2023). De-centralizing the Central Dogma: mRNA translation in space and time. Mol Cell *83*, 452-468. 10.1016/j.molcel.2022.12.030.
77. Garza-Lombo, C., Schroder, A., Reyes-Reyes, E.M., and Franco, R. (2018). mTOR/AMPK signaling in the brain: Cell metabolism, proteostasis and survival. Curr Opin Toxicol *8*, 102-110. 10.1016/j.cotox.2018.05.002.
78. Roach, P.J. (2011). AMPK -> ULK1 -> autophagy. Mol Cell Biol *31*, 3082-3084. 10.1128/MCB.05565-11.
79. Dieni, S., Matsumoto, T., Dekkers, M., Rauskolb, S., Ionescu, M.S., Deogracias, R., Gundelfinger, E.D., Kojima, M., Nestel, S., Frotscher, M., and Barde, Y.A. (2012). BDNF and its pro-peptide are stored in presynaptic dense core vesicles in brain neurons. J Cell Biol *196*, 775-788. jcb.201201038 [pii] 10.1083/jcb.201201038.
80. Heyden, A., Ionescu, M.C., Romorini, S., Kracht, B., Ghiglieri, V., Calabresi, P., Seidenbecher, C., Angenstein, F., and Gundelfinger, E.D. (2011). Hippocampal enlargement in Bassoon-mutant mice is associated with enhanced neurogenesis, reduced apoptosis, and abnormal BDNF levels. Cell Tissue Res *346*, 11-26. 10.1007/s00441-011-1233-3.
81. Hoffmann-Conaway, S., Brockmann, M.M., Schneider, K., Annamneedi, A., Rahman, K.A., Bruns, C., Textoris-Taube, K., Trimbuch, T., Smalla, K.H., Rosenmund, C., et al. (2020). Parkin contributes to synaptic vesicle autophagy in Bassoon-deficient mice. Elife *9*. 10.7554/eLife.56590.
82. Montenegro-Venegas, C., Fienko, S., Anni, D., Pina-Fernandez, E., Frischknecht, R., and Fejtova, A. (2021). Bassoon inhibits proteasome activity via interaction with PSMB4. Cell Mol Life Sci *78*, 1545-1563. 10.1007/s00018-020-03590-z.
83. Annamneedi, A., Caliskan, G., Muller, S., Montag, D., Budinger, E., Angenstein, F., Fejtova, A., Tischmeyer, W., Gundelfinger, E.D., and Stork, O. (2018). Ablation of the presynaptic organizer Bassoon in excitatory neurons retards dentate gyrus maturation and enhances learning performance. Brain structure & function *223*, 3423-3445. 10.1007/s00429-018-1692-3.

84. Schattling, B., Engler, J.B., Volkmann, C., Rothammer, N., Woo, M.S., Petersen, M., Winkler, I., Kaufmann, M., Rosenkranz, S.C., Fejtova, A., et al. (2019). Bassoon proteinopathy drives neurodegeneration in multiple sclerosis. Nat Neurosci *22*, 887-896. 10.1038/s41593-019-0385-4.
85. tom Dieck, S., Kochen, L., Hanus, C., Heumuller, M., Bartnik, I., Nassim-Assir, B., Merk, K., Mosler, T., Garg, S., Bunse, S., et al. (2015). Direct visualization of newly synthesized target proteins in situ. Nat Methods *12*, 411-414. 10.1038/nmeth.3319.
86. Konagaya, Y., Terai, K., Hirao, Y., Takakura, K., Imajo, M., Kamioka, Y., Sasaoka, N., Kakizuka, A., Sumiyama, K., Asano, T., and Matsuda, M. (2017). A Highly Sensitive FRET Biosensor for AMPK Exhibits Heterogeneous AMPK Responses among Cells and Organs. Cell Rep *21*, 2628-2638. 10.1016/j.celrep.2017.10.113.
87. Schindelin, J., Arganda-Carreras, I., Frise, E., Kaynig, V., Longair, M., Pietzsch, T., Preibisch, S., Rueden, C., Saalfeld, S., Schmid, B., et al. (2012). Fiji: an open-source platform for biological-image analysis. Nat Methods *9*, 676-682. 10.1038/nmeth.2019.

## STAR Methods

Resource availability

Lead contact

Further information, inquiries and requests for all reagents and resources should be directed to and will be fulfilled by the lead contact, Michael R. Kreutz (kreutz@lin-magdeburg.de).

Materials availability

All unique reagents (e.g. recombinant DNA) generated in this study are available from the lead contact without restriction.

## EXPERIMENTAL MODEL AND STUDY PARTICIPANT DETAILS

Experimental models

*Rat*

Animals were maintained in the animal facility of the Leibniz Institute for Neurobiology, Magdeburg (Germany) or ZMNH, Hamburg (Germany) under controlled environmental conditions.

All animal experiments have complied with all ethical regulations for animal testing and research in accordance with the European Communities Council Directive (2010/63/EU) and were approved by the ethics committees of Sachsen-Anhalt/Germany (reference number 42502-2-1264 LIN and 42502-2-1284 UNIMD) or of the city-state of Hamburg (Behörde für Gesundheit und Verbraucherschutz, Fachbereich Veterinärwesen) and the animal care committee of the University Medical Center Hamburg-Eppendorf.

*Mouse*

Breedings of animals and experiments using animal material were carried out in accordance with the European Communities Council Directive (2010/63/EU) and approved by the authorities of the State of Saxony-Anhalt (Landesverwaltungsamt Halle) to LIN (TVA $N_{0.}$: 42502-2-1797 LIN).

Preparation primary hippocampal neurons

*Rat*

All animal procedures complied with the ARRIVE guidelines, adhered to EU regulations, and were approved by the relevant institutional ethics committees. Sprague–Dawley rats were maintained in the animal facility of the Universitätsklinikum Hamburg-Eppendorf under standard housing conditions with

unrestricted access to food and water. Experimental protocols were authorized by the local authorities of the State of Hamburg (Org 886; Nr. 125/17).

Primary hippocampal neurons were isolated from E18–E19 rat embryos of both sexes. Following decapitation, hippocampi were dissected in ice-cold HBSS (Sigma, H9269) and rinsed five times in the same solution. Tissues were then digested with trypsin (ThermoFisher, 25200056) at 37 °C for 15 min, washed repeatedly with pre-warmed complete medium [DMEM (ThermoFisher, 41966029) supplemented with 1% L-glutamine (ThermoFisher, 25030024), 1% penicillin–streptomycin (Gibco, 15240062), and 10% FBS (Capricorn, 10-FBS-16F)], and subsequently dissociated mechanically using a 0.90 × 40 mm needle (Sterican, SI10617-01) followed by a 0.45 × 25 mm needle (Sterican, SI10617-18). The resulting cell suspension was filtered through a 100 µm strainer (Greiner, 542000), counted, and diluted in complete medium.

Cells were seeded at a density of 60,000 per 18 mm poly-L-lysine–coated coverslip (Merck, P2636-25MG) and incubated at 37 °C, 5% $CO_2$. After 1 h, the plating medium was replaced with BrainPhys (StemCell, 05790) supplemented with SM1 (StemCell, 05711) and L-glutamine (ThermoFisher, 25030024). Neuronal cultures were maintained under these conditions, fed at DIV7 with an additional 200 µL of supplemented BrainPhys, and used for experiments between DIV14–16.

*Mouse*

For the preparation of hippocampal cultures from neonatal (P0-P1) Sipa1/2-/-, $Bsn^{KO}$, and their respective WT littermates, newborn animals were sacrificed. Their brains were removed, and hippocampi were freed of meninges, plated one pair per 1.5 ml of Hibernate-A medium supplemented with 0.5 mM GlutaMAX™ and 2% B27 in a 2 ml Eppendorf tube, and stored at 4°C until PCR identified WT and KO animals.

Hippocampal tissue was treated with a final concentration of 0.25% trypsin, and the cell suspension was obtained by mechanical trituration. Cells were plated in DMEM with 10% FCS (fetal calf serum), 1mM glutamine, and antibiotics (100U/ml penicillin,100 ug/ml streptomycin at densities of 70.000-80.000 cells per coverslip (18 mm diameter). One hour after plating, the media were changed to Neurobasal A medium supplemented with 2% (v/v) B27, 1 mM sodium pyruvate, 4 mM GlutaMAX™, and antibiotics (100 U/ml penicillin, 100 µg/ml streptomycin).

All neurons were maintained at 37°C in a humidified incubator containing 5% $CO_2$. Cells were used for experiments between 14-16 DIV.

*Sample size estimation*

No formal statistical power calculation was performed, as sample sizes were not determined based on a predefined effect size. Instead, multiple independent experiments were conducted, each including the number of biological replicates indicated in the corresponding figure legends.

**METHOD DETAILS**

Generation of KO animals

Sipa1/2-/- mice were generated as previously described [20]. To generate the constitutive knockout of the SPAR2/sipa1l2 locus (Gene ID: 244668; RefSeq: NM_001081337.1 [mRNA], NP_001074806.1 [protein]), exon 2 was replaced by an IRES-LacZ reporter gene followed by a neomycin phosphoribosyltransferase selection cassette using homologous recombination. The targeting vector was constructed by amplifying the homologous arms from 129S6/SvEv mouse genomic DNA.

Gene targeting was carried out in CCB embryonic stem (ES) cells (129S6/SvEv background). Chimeric mice were generated by injection of correctly targeted ES cells into C57BL/6 blastocysts. Experiments performed with this strain used heterozygous mic that had been backcrossed for 20 generations to the C57BL/6J background and then bred in a 2:1 ratio.

For genotyping, PCR was performed with primers yielding a 200 bp band for the wild-type allele and a 400 bp band for the knockout allele.

To generate the constitutive $Bsn^{KO}$ ($Bsn^{tm2Linmd}$) mice, $Bsn2^{lx/lx}$ ($Bsn^{tm1Linmd}$) mice were crossed with a strain expressing ubiquitously Cre controlled by the CMV promoter, which resulted in Cre-mediated recombination in the germ line. Deletion of the exon 2 of the *Bsn* gene disrupts the reading frame of all exons downstream of exon 1, generating a premature stop codon and loss of the *Bsn* gene expression ([83,84]). To obtain the respective $Bsn^{KO}$ and WT animals for our studies, heterozygous animals were backcrossed for 21-22 generations to the C57BL/6N background and then bred

in a 2:1 ratio. For primary neuronal culture preparations and all other experiments, animals of both sexes were used.

*Plasmid DNA purification*

Mini DNA purification was carried out by the alkaline lysis method. Overnight cultured bacteria were centrifuged for 5 min at 1000 x g and the pellet was resuspended in P1 buffer by vortexing. After the addition of P2 buffer, the tubes were incubated for 5 min at RT. P3 buffer was then added and after another 10 min incubation step at RT, the tubes were centrifuged at 16000 x g for 5 min at 4°C. 500 µl of the supernatant were transferred to isopropanol, incubated at RT for 10 min and centrifuged again as before. The pellet was washed with 70 % ethanol, centrifuged and then air-dried before solving the DNA in 30 µl Tris-HCl (pH 8.0). For large-scale DNA extraction, the NucleoBond Xtra Midi EF kit was used according to the manufacturer's instructions.

*Transfections*

Transfections were carried out simultaneously for both mouse and rat primary hippocampal neurons. DNA and Lipofectamine 2000 were each diluted in either BrainPhys medium for rat neurons or Neurobasal medium for mouse neurons. The DNA and Lipofectamine solutions were then combined at a 1:2 ratio and incubated for 20 minutes at room temperature. Prior to transfection, the conditioned culture medium was collected from each well and replaced with prewarmed BrainPhys or Neurobasal medium, corresponding to the species. The DNA:Lipofectamine complexes were added to the neurons, followed by a 45-minute incubation at 37°C. Subsequently, the transfection mixture was removed and the original conditioned medium was returned to the cells. Only the constructs for the AMPK-dominant negative were transfected 72h prior fixation, other than that all constructs were overexpressed 14-16 hours.

*Immunocytochemistry (ICC)*

The cells were fixed in 4 % paraformaldehyde (PFA) + 4 % (w/v) sucrose for 15 min at RT, washed with PBS and permeabilized with 0.2 % Triton-X100 in PBS for 10 min. After blocking in blocking solution (2 % glycine, 2 % BSA, 0.2 % gelatine and 50 mM $NH_4Cl$ in PBS), the primary antibody was incubated overnight at 4°C diluted in

blocking solution. After three washing steps with PBS, the cells were incubated for 1 h in secondary antibody diluted in blocking solution at RT and, following another three washes with PBS, mounted in Mowiol (10 % (w/v) Mowiol, 25 % (v/v) glycerol, 100 mM Tris-HCl, pH 8.5, 2.5 % (w/v) 1,4-Diazabicyclo[2.2.2]octane).

Experimental methods and confocal image acquisition

*High frequency stimulation*

Electrical field stimulation was carried out using two platinum electrodes placed on the coverslip at a distance of 10mm. Cells were placed in field-stimulation chamber (RC-49MFSH; Warner Instruments, USA) and extracellular stimuli of 900 pulses (1ms; 90mA) were triggered at 10Hz frequency by an isolated pulse generator (MASTER-8, A.M.P.I., Israel) and delivered via a stimulus isolator unit (ISO-Flex, A.M.P.I.). Experiments were performed at DIV 15-16. Coverslips were either electrically stimulated or treated with tetrodotoxin (TTX, hellobio, HB1035-1, 1µM for 1h) for comparison. In the TTX-treated group, 1µM TTX was added to the neuronal growing medium (BrainPhys supplemented with SM1 and glutamine) for 1h and cells were kept in the incubator. Afterwards coverslips were taken out and incubated with 250µL growing medium containing TTX for 90sec. Cells corresponding to the electrically-stimulated group were stimulated in the stimulation chamber containing 250µL of neuronal growing medium for 90 sec. Cells for basal condition were not treated at all. After stimulation, all coverslips were place in the incubator at 37 ºC, 5% CO2. Incubation time was adjusted to experimental question - e.g. for autophagy induction experiments, incubation time was 15 min, for autophagosome/ amphisome quantifications in axons, 30 min. Cells were then fixed in 4% PFA 4% saccharose for 20 minutes.

*Application of reagents and pharmaceutical drugs*

Reagents were added to the culture medium after cell silencing (in the case of TTX treatment), but prior to stimulation (for HFS condition), and remained in the medium until fixation. This procedure was applied consistently across all experiments, regardless of the experimental conditions. For Compound C (171260-5MG, Merck), 50µM was used for 30 min incubation. SBI-0206965 *(*SML1540-5MG, Sigma), was applied for 2 hours. Human TrkB Fc *bodies (NT2-H5254, ACROBiosystems,500ng/m)* and TAT-peptides (30µM) were applied to the well the

day before and incubated overnight. Respectively to the experiment cells were incubated 15 or 30 min. For quantum dot experiments, a coupling mix was prepared with 1µM Quantum Dots (Q10121MP, ThermoFisher), 1µM biotin-BDNF (B-250-B, Alomone) in 1%BSA in PBS. This was vortexed for 20 minutes on low speed. 2mM of Quantum dots concentration was used in culture medium for each well. Cell were incubated 5 min prior stimulation. For stimulating the cells culture medium containing Quantum dots was used and washed away immediately after by using a quencher in tyrodes buffer. Coverslips were incubated for 30 min then fixed and processed for imaging. For experiments with dextran uptake, first TTX group was treated 1h with 1µM TTX in culture medium. Afterwards cells were incubated 5 min prior to stimulation 50µM dextran (D1845, ThermoFisher) in tyrodes buffer (134 mM NaCl, 12 mM NaHCO3, 3 mM KCl, 0.34 mM Na2HPO4, 1 mM MgCl2, 10 mM HEPES, pH 7.4) with 4mM AP5 and 10mM CNOX reagents, on parafilm. For TTX group 1µM TTX was added to dextran solution and just left on parafilm. For stimulation, cells were covered in 250µl of dextran with tyrodes buffer solution during high frequency stimulation in field-stimulation chamber as described previously. Afterwards all coverslips were washed in tyrodes buffer, TTX group with TTX (1µM) respectively. Depending on the experiment, cells were incubated 10 or 30 min with 37 degrees. Independently of the treatment all cells were then fixed in 4% PFA 4% saccharose for 20 minutes and further processed with immunocytochemistry for imaging as described previously.

Images of fixed primary neurons were acquired with an Olympus Fluoview FV3000 microscope using an oil-immersion objective (60X/1.40). Stack images were acquired with a 79x79nm pixel size, a 512x512 or 1024x1024 resolution and a Z-step of 0.30µm. Images were acquired using the 405, 488, 568 and 633 nm laser lines. Imaged axons were chosen based on specific morphological features as follows: (i) elongated, slender processes extending distally from the cell body while maintaining a uniform diameter; (ii) absence of repeated branching along the axon; and (iii) lack of any protrusions or spines along the length of the process. Image acquisition settings were optimized and kept constant for all images between groups of one data set.

<u>Metabolic labeling assays</u>

*Puromycilation*

For puromycylation assays, neurons were incubated with 2 µM puromycin for 5 min in culture medium at 37 °C in a humidified atmosphere with 5 % CO2. After Coverslips were stimulated in presence of puromycin in 250µl culture medium that was just taken out the well, respectively. Cells were incubated 10 min poststimulation and then fixed. Control cells underwent the same treatment but in the absence of puromycin. Immunocytochemistry was performed with other cell markers and prelabelled anti- puromycin-antibody (MABE343-AF647, Sigma).

*FUNCAT-AHA*

The FUNCAT part of the assay was performed as described previously in[85] with following modifications: Cells were preincubated 15 min in methionine-free SILAC medium supplemented with 4mM AHA then stimulated with high frequency stimulation. For experiments with Fc bodies, these were added into the culture medium the day before. Post stimulation incubation time for intensity measurements of AHA at boutons was 10 min and for FUNCAT-PLA experiments, samples were incubated 20 min. Subsequently, cells were washed two times for 5 min with PBS (1× PBS, pH 7.4) and fixed for 15 min in PFA-sucrose (4% paraformaldehyde, 4% sucrose in PBS) at room temperature, washed, permeabilized with 0.5% Triton X-100 in 1× PBS, pH 7.4, for 10 min and blocked with blocking buffer for 1 h. Afterwards cells were equilibrated by two washes with 1 x PBS (pH 7.8) to start CuAAC click reaction.

The reducing agent tris(2-carboxyethyl)phosphine (TCEP) in combination with CuSO4 was used to generate the Cu(I) catalyst for CuAAC, and avoid copper bromide-derived precipitates. A click reaction mix composed of 200 µM triazole ligand Tris[(1-benzyl-1H-1,2,3-triazol-4-yl)methyl]amine (TBTA), 25 µM biotin alkyne tag, 500 µM TCEP and 200 µM CuSO4 was mixed in PBS, pH 7.8. Every reagent was added step by step with intense vortexing in between. The click reaction mixture was prepared immediately before application to the cells and CuAAC was performed overnight at room temperature and then washed with PBS and 0.5 % Triton in PBS, permeabilized and further processed eather as described in the sections ‘FUNCAT-PLA’ or ‘immunocytochemistry’.

*FUNCAT-Proximity ligation assay (PLA)*

For proximity ligation assay, anti-biotin in combination with protein-specific antibodies were used. Detection was carried out with Duolink reagents according to manufacturer's protocol with slight modifications to dilutions. For secondary antibodies, Duolink rb PLAplus and ms PLAminus probes were used. The 'Duolink Detection reagents Red' were used for ligation, amplification and label probe binding. Briefly, after metabolic labeling, permeabilization and washing (see section 'FUNCAT') cells were blocked in blocking buffer (4 % goat serum in PBS, 1 h) and incubated with primary antibody pairs diluted in blocking buffer (1.5 h at room temperature). After washing, PLA probes were applied in 1:10 dilution in blocking buffer for 1 h at 37 °C, washed several times with wash buffer A (0.01 M Tris, 0.15 M NaCl, 0.05 % Tween20) and incubated for 30 min with the ligation reaction containing the circularization oligos and T4 ligase prepared according to the manufacturer's recommendations (Duolink Detection reagents Red, Sigma) in a prewarmed humidified chamber at 37 °C. Amplification and label probe binding was performed after further washes with wash buffer A with the amplification reaction mixture containing Phi29 Polymerase and the fluorophore-labeled detection oligo prepared according to the manufacturer's recommendations (Duolink Detection reagents Red, Sigma) in a prewarmed humidified chamber at 37 °C for 100 min. Amplification was stopped by three washes in 0.2 M Tris, 0.1 M NaCl pH 7.5 followed by washes in PBS pH 7.4. For better signal stability, cells were postfixed for 10 min at room temperature in PFA-sucrose, washed with PBS and processed further for immunohistochemistry. After staining, imaging, quantification and analysis was conducted as described in previous section.

*Live-imaging of AMPK-activity sensor*

Primary neurons (DIV14-15) were transfected with GFP-AMPK-DN or GFP as control 48h prior before the experiment was performed. Images were acquired in a scanning confocal microscope (Leica TCS SP8 X) controlled by the software Leica LAS X, using HCX PL APO63x1.40 objective. Cells were imaged in an environmental chamber prewarmed at 37ºC. The following laser lines were using for illumination: 415nm for CFP; 530nm for YFP and 561nm for Sphy-tRFP. Images were acquired in a sequential manner every 20 seconds. HFS stimulation was performed 2 minutes after baseline acquisition.

*STED*

Stimulated emission depletion (STED) imaging was carried out using an Abberior multichannel confocal/STED microscope based on a Nikon Ti-E microscope body with perfect focus system controlled by Imspector Software (Abberior Instruments). An x60 P-Apo oil immersion objective (NA 1.4) was used. STED laser lines 561 and 640nm were used for excitation and a laser line at 775nm was used for fluorescence depletion.

*DNA-PAINT/MINFLUX*

Primary neurons at DIV14-16 were stimulated using HFS and kept in the incubator at 37ºC 5%CO2 for 30 minutes. After fixation with 4% PFA, immunocytochemistry was performed as described above using mouse-anti LC3 (1:300; MBL) and rabbit anti-pTrk (1:300). Samples were incubated with the following secondary antibodies for one hour at room temperature: anti-mouse 488 (1:500); anti-mouse MF4 (1:200); anti-rabbit MF5 (1:500). Following secondary-antibody labeling, coverslips were washed with PBS for 3 times and kept in PBS at 4ºC until the experiment was performed.

Sample preparation before imaging was performed using the MASSIVE-DNA-PAINT kits optimized for MINFLUX microscopy (Abberior) according to manufacturer´s instruction. Gold nanorods (Nanopartz Inc) were used as fiducials and were applied to the coverslips for 5 minutes followed by a 15-minute treatment with poly-L-lysine. Right before imaging, samples were incubated with imager strands (MF4 1:1000; MF5 1/2000) which were diluted in PBS, and mounted on dimple slides sealed with two-part silicon glue for easy imaging and storage.

MINFLUX nanoscopy, corresponding confocal imaging as well as image rendering were performed in a MINFLUX setup as previously described[35].

Following acquisition, single-molecule localizations were filtered. Localizations that were found in >4 scans were taken into consideration. Images were visualized using Fiji and IMARIS.

## QUANTIFICATION AND STATISTICAL ANALYSIS

*Image analysis*

The analysis was conducted using the free software Fiji (ImageJ). Maximum intensity projections of the raw image stacks were generated for quantification. For intensity

measurements, the thresholding function in ImageJ was applied to define regions corresponding to presynaptic antibody labeling. Integrated density values within these regions were quantified to compare TTX and stimulated groups. For colocalization analysis, the thresholding function was first used to mask imaged axons, followed by identification of signals from labeled proteins of interest. Consistent threshold values were applied across the same channels in different experimental groups. Regions of interest (ROIs) were counted using the multi-point tool. Colocalization events were defined by the overlap of ROIs from different channels and saved as RoiSets.

*Statistical analysis*

Statistical Analysis was performed with GraphPad Prism 10. Simple t-test was used to compare 2 unpaired samples.One way ANOVA was used to compare more than two groups, for analysis of wildtype/ko animals, two-way ANOVA was conducted. Use of asterisks: p-value: <0.0001 to 0.001 ***, 0.001 to 0.01 **, 0.01 to 0.05 *, ≥ 0.05 not significant (ns).

Data in the manuscript are shown as mean ± SEM and *n* numbers used for statistics are depicted in each panel or figure legends. Graphs and statistical analysis was made with GraphPad Prism (GraphPad Software).

## KEY RESOURCES TABLE

| REAGENT or RESOURCE | SOURCE | IDENTIFIER |
|---|---|---|
| Antibodies | | |
| Synaptophysin1 antibody (guinea pig) | Synaptic Systems | 101 308 |
| LC3 (mouse) | MBL | M152-3 |
| pATG16L1 (pS278) (rabbit) | Abcam | ab195242 |
| Biotin (mouse) | Sigma-Aldrich | B7653 |
| pTrkB / pTrkA (rabbit) | Cell Signaling | 9141 |
| RPS3A (rabbit) | Proteintech | 14123-1-AP |
| Tau (guinea pig) | Synaptic Systems | 314 004 |
| Anti-Cathepsin D (rabbit) | Abcam | ab72915 |
| Homer1b/c (chicken) | Synaptic Systems | 160 019 |
| RPL10A (rabbit) | Proteintech | 16681-1-AP |
| Piccolo (guinea pig) | Synaptic Systems | 142 104 |
| LAMP2A (mouse) | Synaptic Systems | 437 005 |
| Biotin (rabbit) | Biomol | A150-109A |
| ULK1 (rabbit) | Cell Signaling | 8054 |
| Tau (chicken) | Synaptic Systems | 314 006 |
| Synapsin 1/2 (rabbit) | Synaptic Systems | 106 002 |
| LC3 (rabbit) | Abcam | ab192890 |
| Bassoon (mouse) | Enzo | SAP7F407 |
| Bassoon (guinea pig) | Synaptic Systems | 141 318 |
| Wipi ½ (mouse) | Abcam | ab128901 |
| SQSTM1/p62 (mouse) | Abcam | ab 56416 |
| Biotin (mouse) | Sigma Aldrich | B7653 |
| Anti-Puromycin Conjugated 647, clone 12D10 (mouse) | Sigma-Aldrich | MABE343-AF647 |
| Tau AB Conjugated 488 (mouse) | Merck | MAB3420A4 |
| GFP-Booster Alexa Fluor 488 | Chromotek | gb2AF488-10 |
| Donkey anti-mouse IgG Alexa Fluor 488 | Invitrogen | A-21202 |
| Donkey anti-mouse IgG Alexa Fluor 647 | Invitrogen | A-31571 |
| Donkey anti-rabbit IgG Alexa Fluor 568 | Invitrogen | A-10042 |
| Donkey anti-guinea pig IgG Alexa Fluor 405 | Abcam | ab175678 |
| Donkey anti-guinea pig IgG Alexa Fluor 488 | Invitrogen | A-11073 |
| Donkey anti-guinea pig IgG Alexa Fluor 647 | Invitrogen | A-21450 |
| Goat anti-chicken IgG Alexa Fluor 405 | Invitrogen | A-48260 |
| Donkey anti-chicken IgG Alexa Fluor 488 | Invitrogen | A-78948 |
| Duolink anti rabbit PLUS | Sigma Aldrich | DUO92002 |
| Duolink anti mouse MINUS | Sigma Aldrich | DUO92004 |
| Bacterial and virus strains | | |
| DH5-alpha | NEB | C2987H |
| E-Coli XL10 gold | Agilent | 200315 |
| Chemicals, peptides, and recombinant proteins | | |
| HBSS | Sigma | H9269 |
| DMEM | ThermoFisher | 41966029 |
| Neurobasal-A medium | ThermoFisher | 10888022 |
| BrainPhys medium | StemCell Technologies | 05790 |
| SM1 supplement | StemCell Technologies | 05711 |
| FBS | Capricorn | 10-FBS-16F |
| GlutaMAX | ThermoFisher | 35050061 |
| L-glutamine | ThermoFisher | 25030024 |

| | | |
|---|---|---|
| Penicillin-Streptomycin | Gibco | 15240062 |
| Poly-L-lysine | Merck | P2636-25MG |
| Trypsin | ThermoFisher | 25200056 |
| Biotin-BDNF | Alomone Labs | B-250-B |
| Compound C | Merck | 171260-5MG |
| SBI-0206965 | Sigma | SML1540-5MG |
| Human TrkB-Fc | ACROBiosystems | NT2-H5254 |
| Tetrodotoxin (TTX) | HelloBio | HB1035-1 |
| Dextran | ThermoFisher | D1845 |
| Paraformaldehyde | Carl Roth | P087.5 |
| D (+)-Saccharose | Carl Roth | 4661.1 |
| HEPES | Merck | H4034 |
| Lipofectamine 2000 | ThermoFisher | 11668019 |
| Fetal calf Serum | Gibco | 10270-106 |
| Antibiotic-Antimyotic | Thermo Fisher | 15240-062 |
| Sodium pyruvate | Thermo Fisher | 11360070 |
| Trypan | Sigma Aldrich | T8154-20ML |
| Dibenzocyclooctyne-PEG4-biotin conjugate | Sigma Aldrich | 760749 |
| Tris(2-carboxyethyl)phosphin -hydrochlorid | Merck | 646547-10X1ML |
| Duolink Detection Reagents Red | Sigma Aldrich | DUO92008 |
| AP5 | HelloBio | HB0225 |
| CNOX | HelloBio | HB0205 |
| 10XPBS | Roth | 9150.1 |
| AHA | Iris Biotech | 120042-14-0 |
| Tris[(1-Benzyl-1H-1,2,3-Triazol-4-yl)methyl]amin | Sigma Aldrich | 678937 |
| Copper(II) sulfate | Sigma Aldrich | 908940 |
| Albumin Fraktion V | Roth | 8076.2 |
| Triton X100 | Carl Roth | 3051.2 |
| Critical commercial assays | Critical commercial assays | Critical commercial assays |
| abberior DNA-PAINT 660, MASSIVE anti-mouse MINFLUX Kit | abberior DNA-PAINT 660, MASSIVE anti-mouse MINFLUX Kit | abberior DNA-PAINT 660, MASSIVE anti-mouse MINFLUX Kit |
| abberior DNA-PAINT 580, MASSIVE anti-rabbit MINFLUX Kit | abberior DNA-PAINT 580, MASSIVE anti-rabbit MINFLUX Kit | abberior DNA-PAINT 580, MASSIVE anti-rabbit MINFLUX Kit |
| Experimental models: Organisms/strains | | |
| Embryonic stem cells (CCB; 129S6/SvEv strain) | CCB | |
| Sprague-Dawley rats, E18 | Charles River / Janvier | |
| C57BL/6J mice | Jackson Laboratory | Stock No. 000664 |
| Sipa1l2 KO mice | Ref.[20] | |
| $Bsn^{KO}$ mice | Ref.[83], Ref.[84] | |
| Oligonucleotides | | |
| TAT-DynI769-784AA (TAT-AA): YGRKKRRQRRRPAGRRAPTSAPTPQRR | Genosphere Technologies Refs.[39,40] | |
| TAT- DynI769–784EE (TAT-EE): YGRKKRRQRRRPAGRREPTSEPTPQRR | Genosphere Technologies Refs.[39,40] | |
| | | |
| | | |

| | | |
|---|---|---|
| Recombinant DNA | | |
| LC3-GFP | | LC3-GFP |
| ER-Ds-Red | Gift from Thomas Oertner's Lab, ZMNH Hamburg | ER-Ds-Red |
| Synapsin-RFP | This paper | Synapsin-RFP |
| Synaptophysin-RFP | Ref.[20] | |
| AMPK-dominant negative<br>AMPK-FRET sensor | Gift<br>Ref.[86] | |
| Mouse GFP-fl-SIPA1L2-1-1722 (pEGFP-C1, Clontech) | | |
| | | |
| Software and algorithms | | |
| Prism Version 9 and 10<br><br>Fiji | Graph Pad<br><br>Ref.[87] | https://www.graphpad.com/scientific-software/prism/<br>https://imagej.net/downloads |
| IMARIS | Bitplane | |
| Imspector Version 16.3.13033-w2049 | Abberior instruments | https://imspector.abberior-instruments.com/ |
| Other | | |
| Quantum dots | ThermoFisher | Q10121MP |
| | | |

## Figures and Figure legends

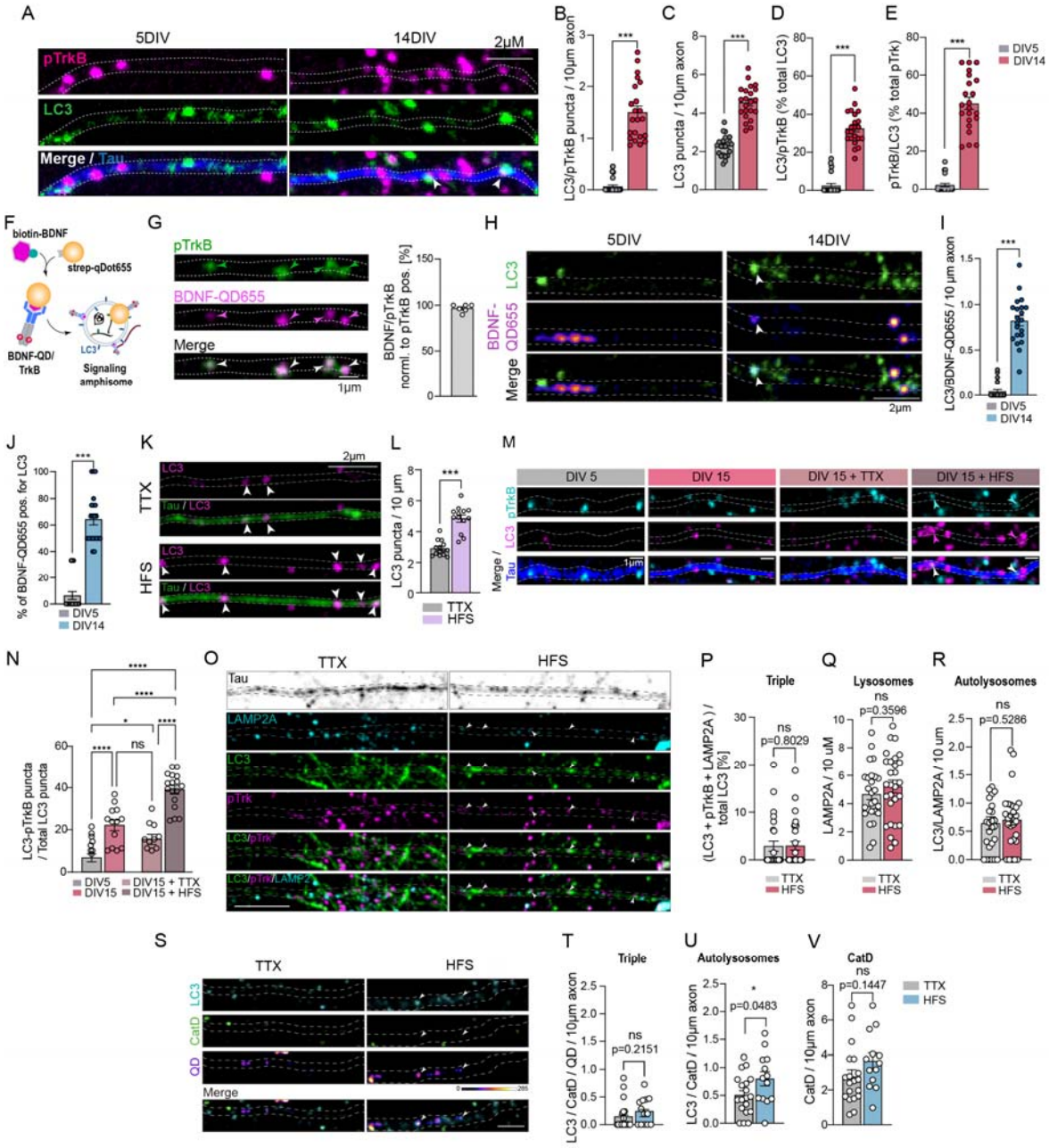


**Figure 1. Signaling amphisomes are segregated from the endo-lysosomal pathway in mature neurons.**

A) Representative images of axons identified by Tau from primary hippocampal neurons at DIV5 and 14 immunostained against pTrk and LC3. Scale bar indicates 2µm.

B) Number of LC3- and pTrkB- double positive puncta in 10 µm axon of neurons at DIV5 and DIV14 from the experiment in A.

C) Bar graph depicting the number of LC3-positive puncta per 10µm of axon obtained from neurons at DIV5 and DIV14 from the experiment in A.

D) Quantification of amphisomes (LC3+pTrkB-positive) in 10µm axon as percentage of the total LC3 from axons at DIV5 and DIV14.
E) Percentage of all pTrkB puncta that colocalize with LC3 puncta in 10µm axon axons at DIV5 and DIV14.
(B-E) *n=22 from 3 independent cultures*
F) Schematic representation of the assay employed to label BDNF/TrkB complexes using biotin-BDNF coupled to streptavidin-QD655.
G) Representative images of primary neurons incubated with BDNF-QD655 and immunostained against pTrkB. Right, bar graph showing the percentage of BDNF-QD655 positive for pTrkB in axons labeled by Tau (not shown, shaded line). *(n=6)*
H) Representative images of endogenous LC3 staining and BDNF-Qdots 655 in axons (depicted with scattered white lines) from primary hippocampal neurons at DIV5 and 14. Scale bar indicates 2µm.
I) Bar graph shows colocalization of LC3 puncta with endogenous BDNF-QD655 per 10µm axon in DIV5 compared to DIV 14. Extracellular signal of QD655 was quenched.
J) Quantification of axonal BDNF-QD655 positive for LC3 puncta as percentage.
(G-H) *n=21 from 3 independent cultures*
K) Representative image of LC3 puncta in axon labeled by Tau in TTX and HFS-stimulated cells.
L) Quantification of experiment in K) showing the amount of LC3 puncta per 10µm axon.
*n=13 (FS) n=14 (TTX) from 3 independent cultures*
M) Representative images of primary neurons immunostained for LC3, pTrkB and Tau in neurons at DIV5 vs. DIV15 neurons under basal conditons as well as DIV15 neurons that were silenced with TTX or stimulated using high-frequency stimulation (HFS).
N) Quantification of amphisomes (pTrkB/LC3-positive) in axons as percentage of total LC3-positive vesicles from the experiment in M. n=*3 independent cultures)*
O) Representative images of endogenous LC3, pTrkB and LAMP2 staining in axons from primary hippocampal neurons at DIV14 comparing TTX and HFS conditions. Scale bar indicates 2µm.
P) Quantification of triple-positive structures (pTrkB+LC3+LAMP2) as percentage of total analyzed LC3.
Q) Quantification of LAMP2A puncta in 10 µm axon.
R) Bar graph shows colocalization of LC3 puncta with LAMP2A puncta per 10 µm axon.
(M-P) *n=28 (FS) n=26 (TTX) from 3 independent cultures*
S) Representative images of endogenous Cathepsin staining and BDNF-Qdots 655 in axons from primary hippocampal neurons at DIV14 comparing TTX and HFS conditions. Scale bar indicates 2µm.
T) Bar graph shows colocalization of Cathepsin and LC3 puncta with endogenous BDNF-QD655 per 10µm axon in DIV 14. Extracellular signal of QD655 was quenched.
U) Bar graph shows colocalization of LC3 puncta and Cathepsin puncta in 10µm axon.
V) Quantification of Cathepsin puncta per 10µm axon.
(P-T) *n=28 (FS) n=13 (TTX) from 3 independent cultures*

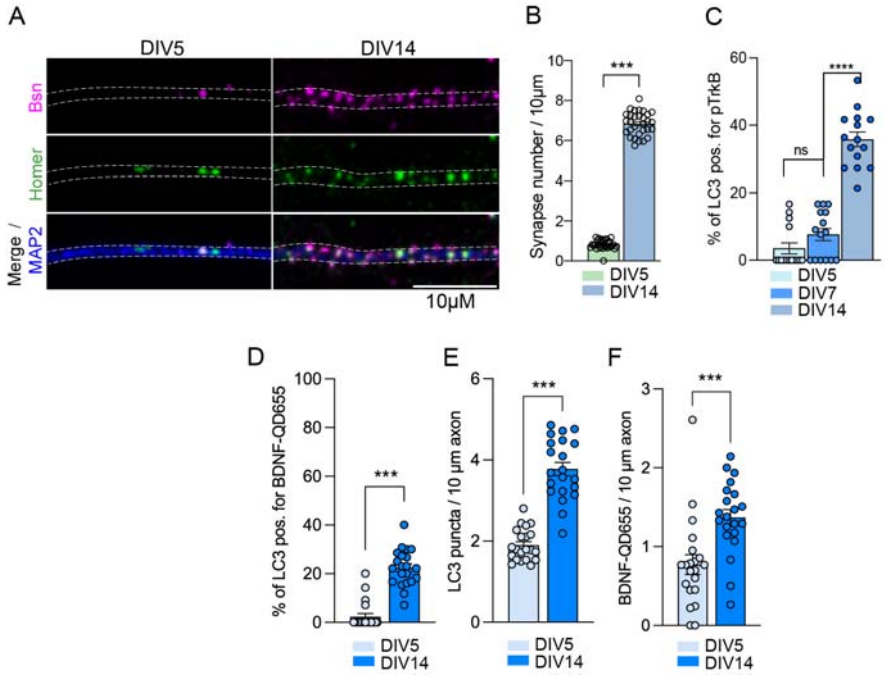


**Figure S1. Amphisome biogenesis occurs in mature neurons**

A) Representative images of neurons at DIV5 and 14 immunostained against MAP2 as neurite marker, and Bassoon and Homer as synaptic markers. Scale bar indicates 10µm.

*B)* Quantification of synapse number from S1A). *n=30 from 3 independent cultures.* Belongs to Fig.1F;

C) Percentage of amphisomes from total LC3-vesicles analyzed in axons from cells at DIV5, DIV7 and DIV14.

D) Percentage of all quantified LC3 puncta colocalizing with BDNF in axons under basal conditions in DIV5 and DIV14 hippocampal neurons. Fig 1H+I

E) Quantification of LC3 puncta in 10 µm axon from the experiment in C/Fig 1H+I

F) Quantification of BDNF-QD655 in 10 µm axon from the experiment in C/Fig 1H+I.

(C-E) *n=21 from 3 independent cultures*

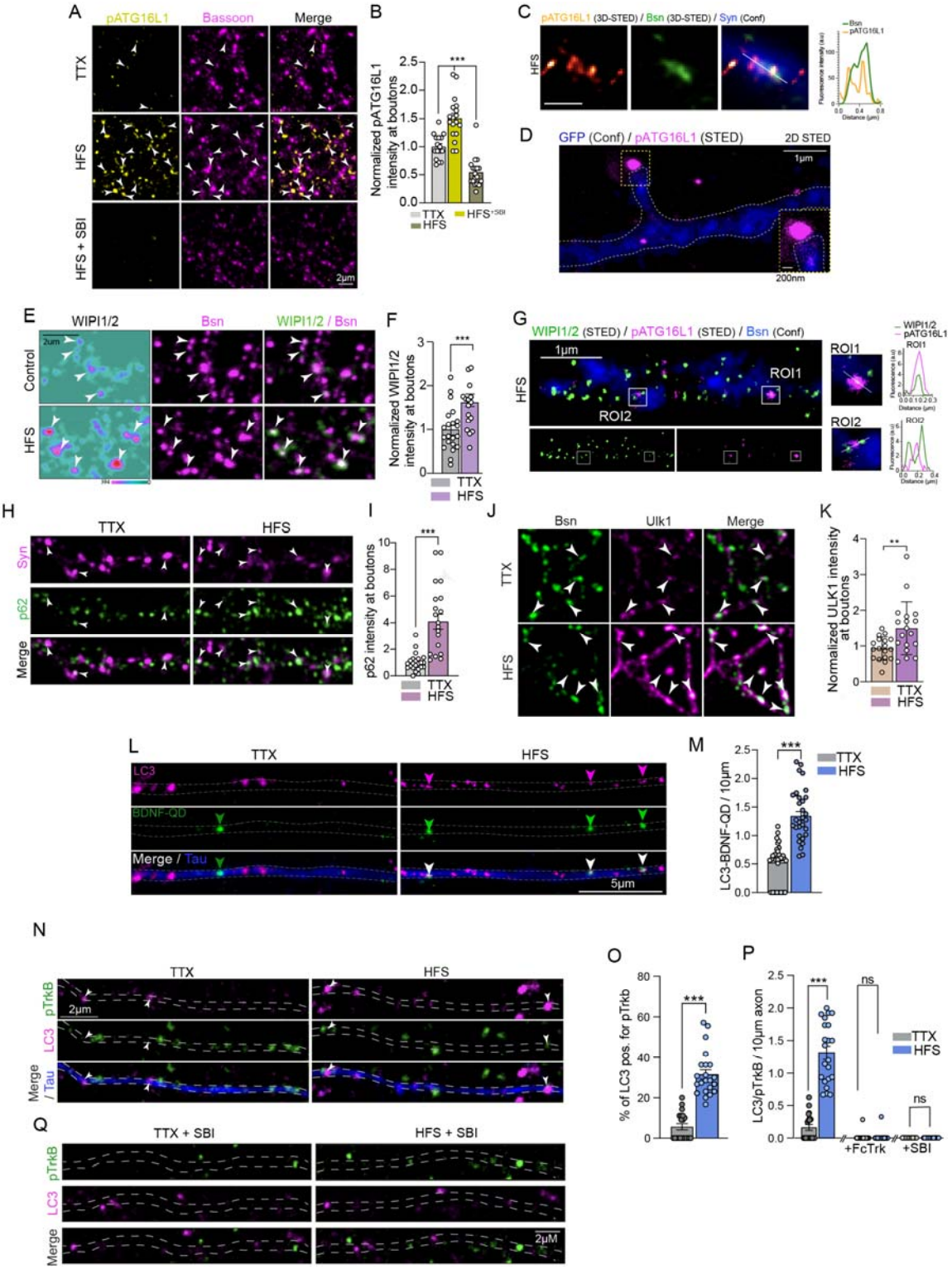


**Figure 2. Electrical field stimulation causes autophagy activation at boutons.**

A) Representative images of TTX or HFS-treated primary neurons immunostained for Bassoon and pATG16L1.

B) Bar graph depicting the intensity of pATG16L1 at the presynapse identified by Bassoon in neurons treated with TTX, HFS and HFS after 2h of treatment with SBI-0206965. *n= 16 (TTX); n= 18 (FS+ FS SBI) from 2 independent cultures*

C) Superresolution 3D STED image of pATG16L1 localizing with the presynaptic scaffold Bassoon. Synapsin signal acquired with confocal microscopy is shown in blue. Left, intensity line profile from the images.
D) 2D STED image displaying GFP as neuronal cell fill, and pATG16L1
E) Representative image of primary neurons immunostained against WIPI1/2 at boutons labelled with presynaptic marker Bassoon. Scale bar indicates 2µm.
F) Quantification of WIPI1/2 intensity at boutons at TTX-treated and HFS groups. *n=18 (FS) n=16 (TTX) from 3 independent cultures*
G) 2D STED image from HFS cells stained for WIPI1/2 and pATG16L1, as well as bassoon in confocal. White squares in main images indicates ROI1 and ROI2 that are zoomed in on the right side accompanied by line profiles showing fluorescence intensity over distance. Scale bar indicates 1µm.
H) Representative images showing immunostaining of primary neurons against p62 and Synapsin as presynaptic marker for TTX and HFS conditions.
I) Bar graph depicts p62 intensity measured at presynapses detected by Synapsin comparing TTX and HFS conditions. *n=21 (FS) n=23 (TTX) from 3 independent cultures*
J) Representative images of the presynapse labelled with Bassoon and Ulk1.
K) Quantification of Ulk1 intensity measured in Bassoon-positive boutons from TTX and HFS groups. *n=18 from 3 independent cultures*
L) Representative images of neurons incubated with BDNF-QD655 and immunostained against LC3. Scale bar indicates 5 µm.
M) Quantification of amphisome number in 10µm axon detected as LC3/ BDNF-QD655. *n=30 from 3 independent cultures*
N) Representative image of primary neurons treated with TTX or HFS and immunostained against LC3, pTrkB and Tau.
O) Quantification of the total percentage of LC3 puncta positive for pTrkB showing the relative amount of amphisomes to autophagosomes in 10 µm axon of TTX vs HFS cells.
P) Number of colocalizing LC3/pTrkB puncta in 10 µm axon in TTX and HFS cells (*n=22 (FS) n=20 (TTX) from 3 independent cultures)* and quantification in cells treated with SBI-0206965 for 2h (*n=16 (FS) n=14 (TTX) from 2 independent cultures*) and Fc Trk overnight (*n=26 (FS) n=25 (TTX) from 3 independent cultures)*, respectively.
Q) Representative image of primary neurons treated with SBI-0206965 and immunostained against LC3, pTrkB and Tau.

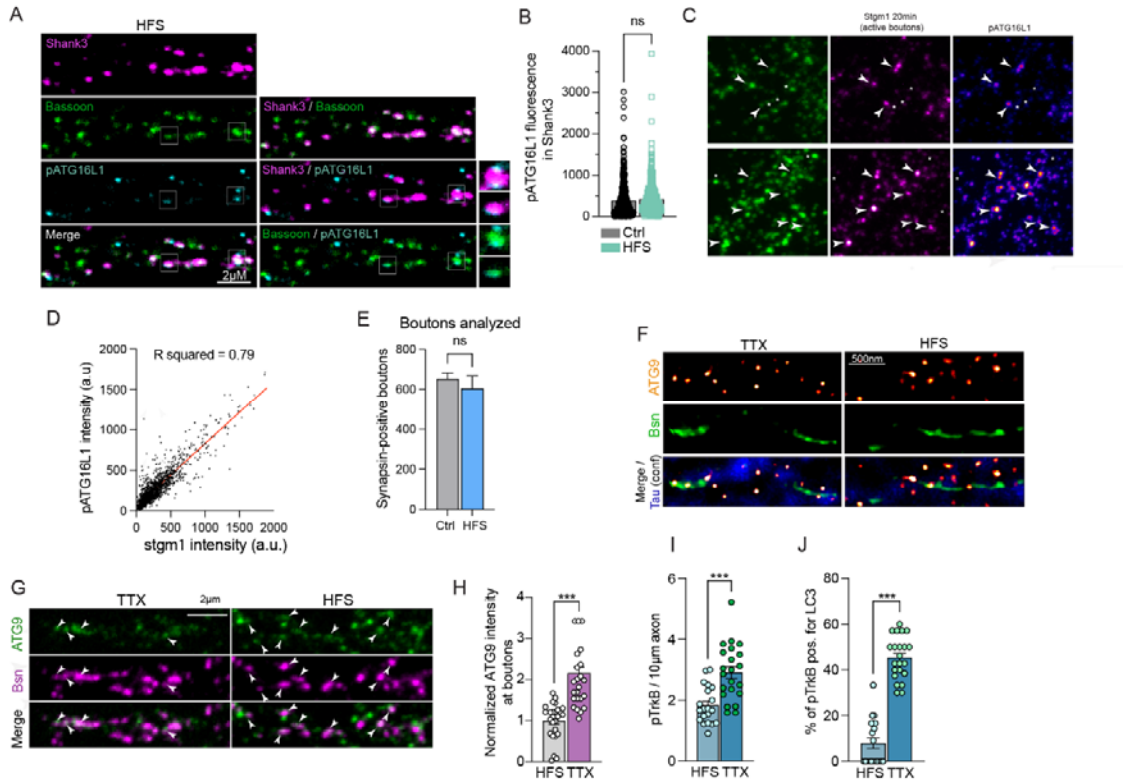


**Figure S2 Electrical field stimulation induces autophagy activation at boutons.**

A) Representative images of TTX or HFS-treated primary neurons immunostained for Shank3, Bassoon and pATG16L1.
B) Quantification of pATG16L1 intensity measured at postsynaptic sites labelled with Shank3 in TTX and HFS neurons.
C) Representative image of primary neurons treated with TTX or HFS in the presence of an anti-synaptotagmin1 (luminal domain) antibody whose epitope is only exposed upon fusion of synaptic vesicles with the plasma membrane. After fixation cells were immunostained against pATG16L1.
D) Correlation analysis of pAtg16l1 intensity to Stgm1 intensity in synapsin mask.
E) Bar graph shows the total number of analyzed boutons for the experiment in C in the HFS and control group.
F) 2D STED image of ATG9 and Bassoon in axons, labelled in blue (confocal) with Tau. Scalebar is 500nm.
G) Representative images of the presynapse labelled with Bassoon and ATG9.
H) Quantification of ATG9 intensity measured in Bassoon-positive boutons from TTX and HFS groups.
I) Quantification of pTrkB puncta in axons. TTX and HFS compared. To Fig2,P.
J) Percentage of pTrkB puncta positive for LC3 in axons. To Fig2,P).

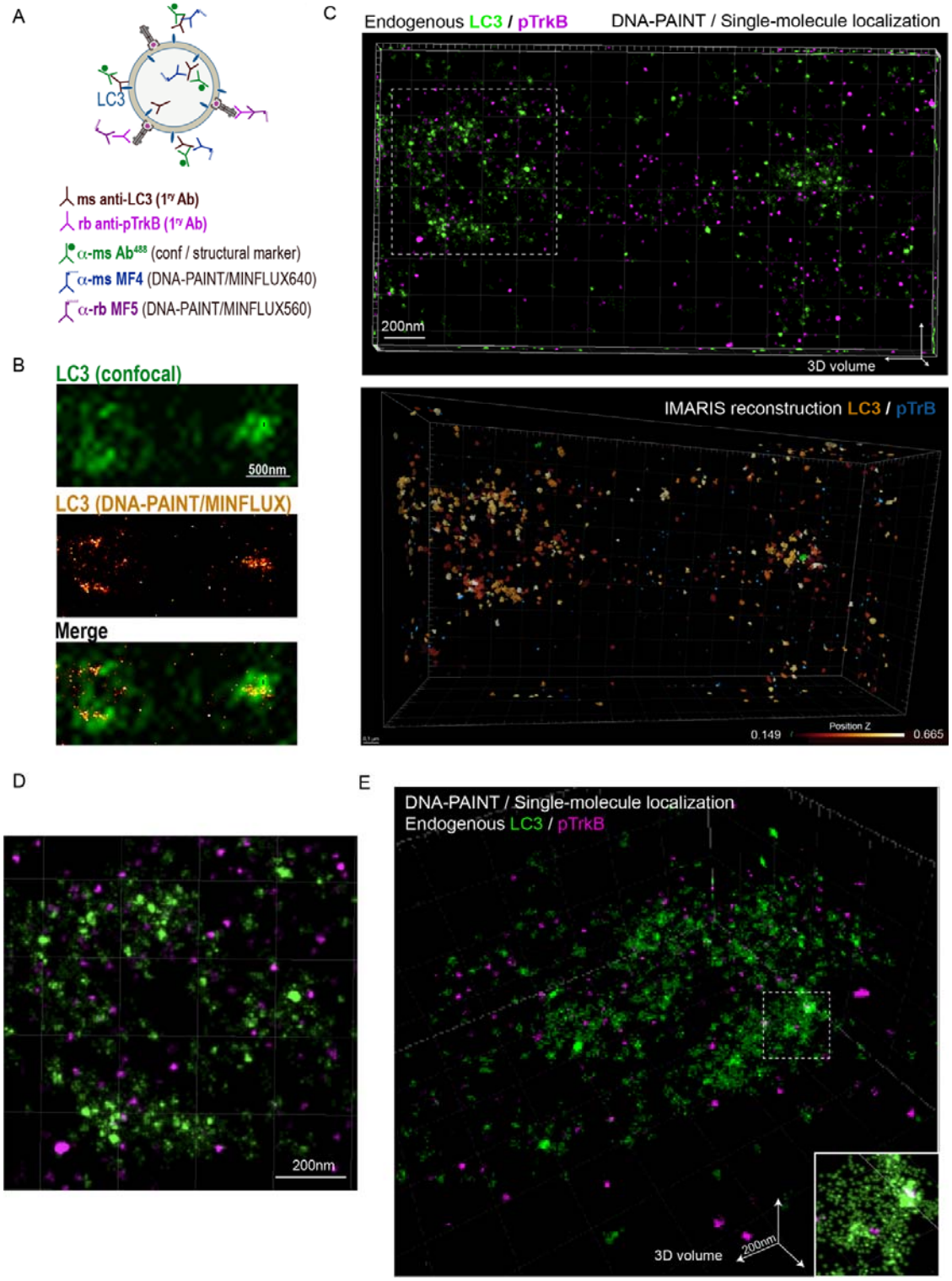


**Figure 3. Ultrastructure of amphisomes revealed by DNA-PAINT/MINFLUX.**

A) Schematic of the experimental approach used in the experiments. Two primary antibodies against LC3 and pTrkB were used in primary neurons stimulated by HFS. Two secondary antibodies against ms LC3 (one used as structural marker and the other one for DNA-PAINT) and one against rb pTrkB were used.

B) Endogenous LC3 imaged by confocal (upper panel) and DNA-PAIN/MINFLUX.

C) 3D volume of single-molecule localizations obtained for endogenous LC3 and pTrkB with DNA-PAINT/MINFLUX. Below, 3D reconstruction of the signal shown above with IMARIS. Z position is color-coded. Scale bar is 200nm.
D) Zoomed image of LC3 and pTrkB 3D localization from ROI (scattered square) shown in C. Scale bar is 200nm.
E) 3D volume plot of single-molecule localizations obtained for LC3/pTrkB. The inset shows the tight association of pTrkB with LC3. Pixel size is 4nm. Scale bar is 200nm.

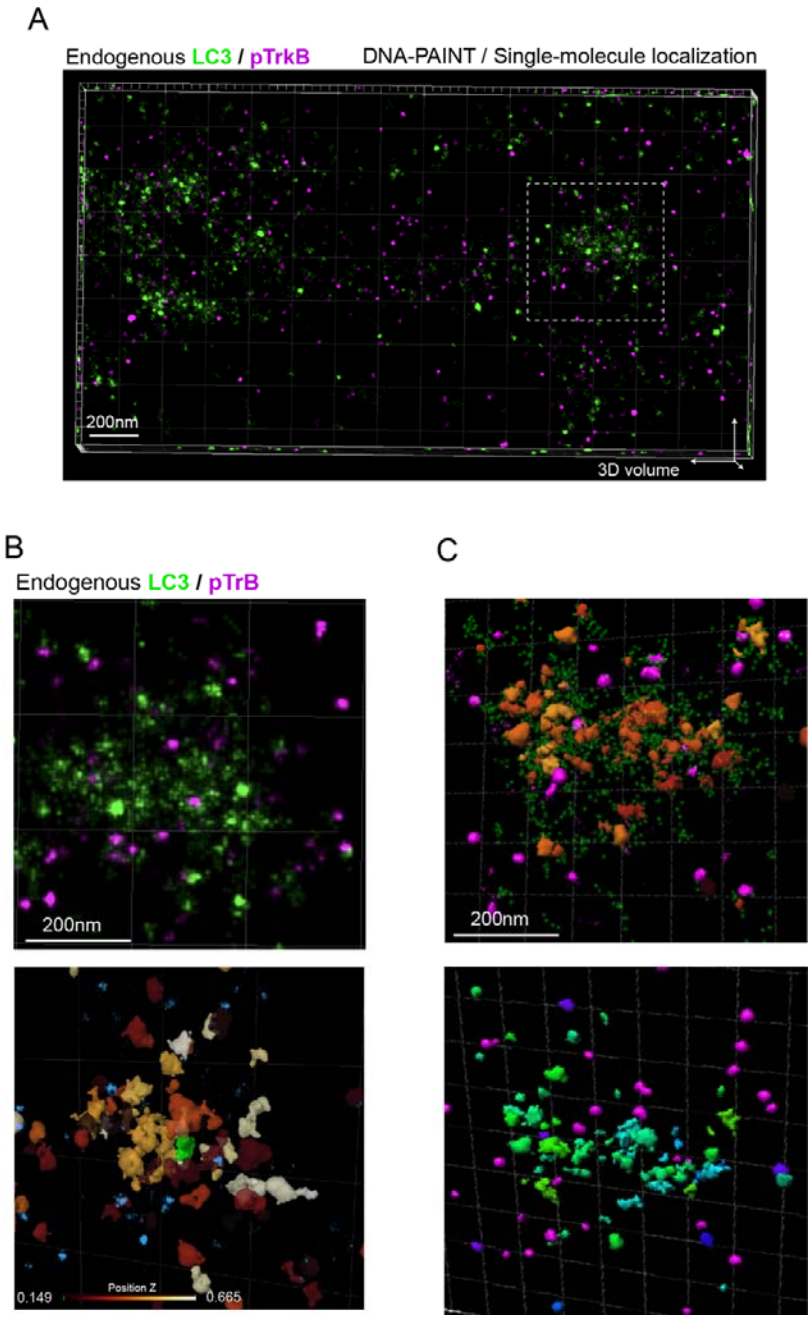


**Figure S3.** ***Single molecule localization of endogenous stained LC3 and pTrkB.***

A) 3D volume of single molecule localizations obtained for endogenous LC3 and pTrkB with DNA-PAINT/MINFLUX. Below, 3D reconstruction of the signal shown above with IMARIS. Z position is color-coded. Scale bar is 200nm

B) Zoomed image of LC3 and pTrkB 3D localization from ROI (scattered square) shown in A. Scale bar is 200nm.

C) A different example from another experiment of an amphisome images by DNA-PAINT/MINFLUX.

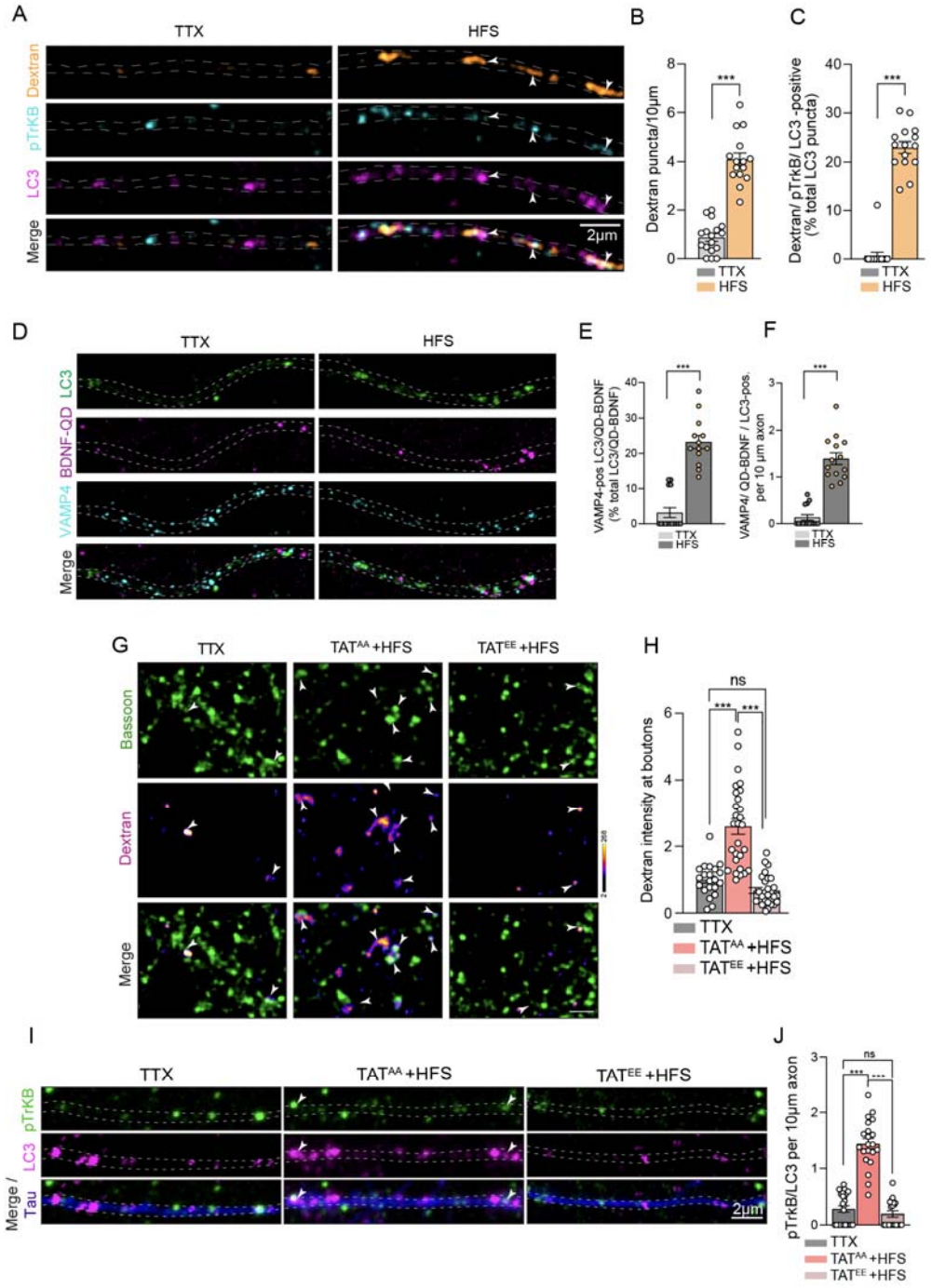


**Figure 4. Amphisomes are formed from bulk-endosomes.**

A) Representative images of primary hippocampal neurons at DIV14 incubated with high-molecular weight Dextran (40kDa) that were either treated with TTX or stimulated by means of HFS in the presence of dextran. Stained for colocalization analysis with amphisomal markers LC3 and pTrkB. Scale bar indicates 2µm.
B) Bar graph shows number of Dextran puncta along 10µm of axon from A.

C) Quantification of the total percentage of analyzed LC3 puncta along axons positive for Dextran in TTX treated to HF-stimulated cells. *n=15 (HFS), n=17 (TTX) from 2 independent cultures*
D) Representative image of neurons at DIV14 labelled with BDNF-QD655 and immunostained for LC3 and VAMP4 for TTX and HFS.
E) Quantification of the total percentage of amphisomes labbeled with BDNF-QD655 and LC3 positive for VAMP4 in 10µm axon of TTX treated to HF-stimulated cells.
*n=13(HFS), n=14 (TTX) from 2 independent cultures*
F) Triple colocalization of VAMP4, Dextran and LC3 relative to total amount of LC3 puncta in percentage.
G) Representative image of primary neurons incubated with Dextran and stimulated in the presence of TAT-AA (mock) or TAT-EE and immunolabeled with the presynaptic marker Bassoon. Scale bar indicates 1µm.
H) Dextran intensity measured at presynapses identified by Bassoon. Quantification to D. n=28 from 3 independent cultures
I) Representative image of axons identified by Tau from primary hippocampal neurons at DIV14 immunostained against pTrkB and LC3. Showing TTX, TAT scrambled (AA) and TAT peptide (EE) treated conditions.
J) Colocalization analysis of pTrkB and LC3 in 10µm axon. Quantification to I). *n=20 (HFS-TAT EE), n=21(TAT AA), n=24 (TTX) from 3 independent cultures*

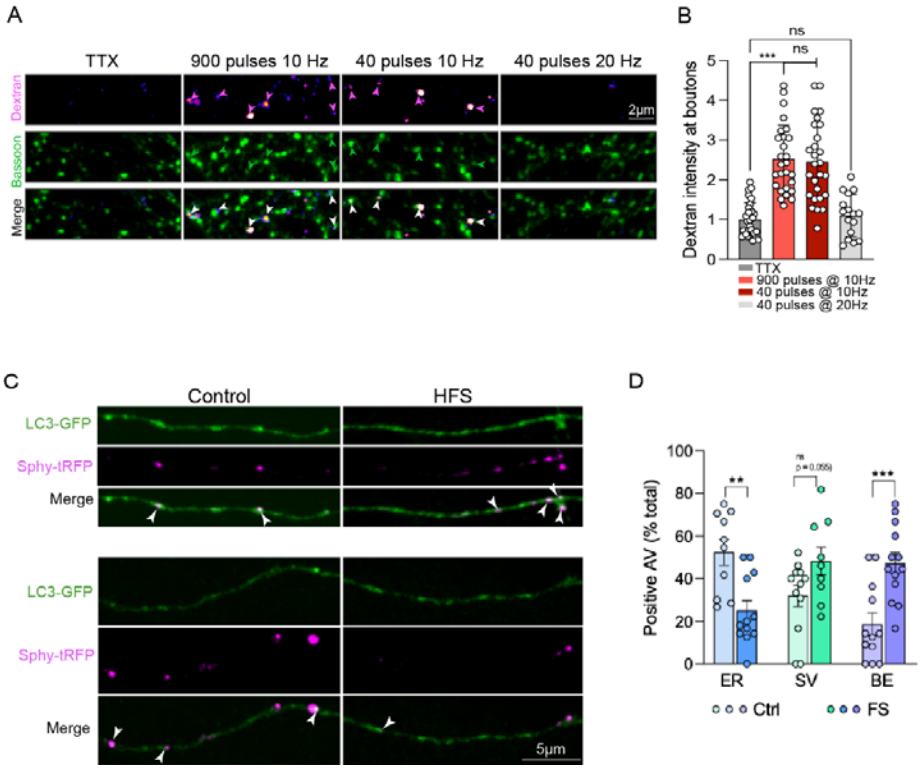


**Figure S4 - Amphisomes are formed from bulk-endosomes.**

A) Representative images showing dextran at puncta detected by Bassoon staining following different electrical stimulation protocols.
B) Bar graph shows dextran intensity at boutons from the experiment in B. TTX group compared to different stimulation protocols. n= 29 (TTX); n=27(HFS); 27(40Hz); n=16(20Hz)
C) Representative images showing LC3-GFP structures positive for either ER-dsRed (ER group), Sphy-RFP (SV group). Representative images for dextran (BE group) in control and HFS groups are shown in Figure 4A.
D) Bar graph shows LC3-positive vesicles positive for the second marker as as percentage of total analyzed LC3-positive structures from the experiment in B. n=10 (ER,TTX); n=128ER,FS); n=12 (SV TTX); n=9 (SV FS); n=12( BE TTX); n= 13(BE FS)

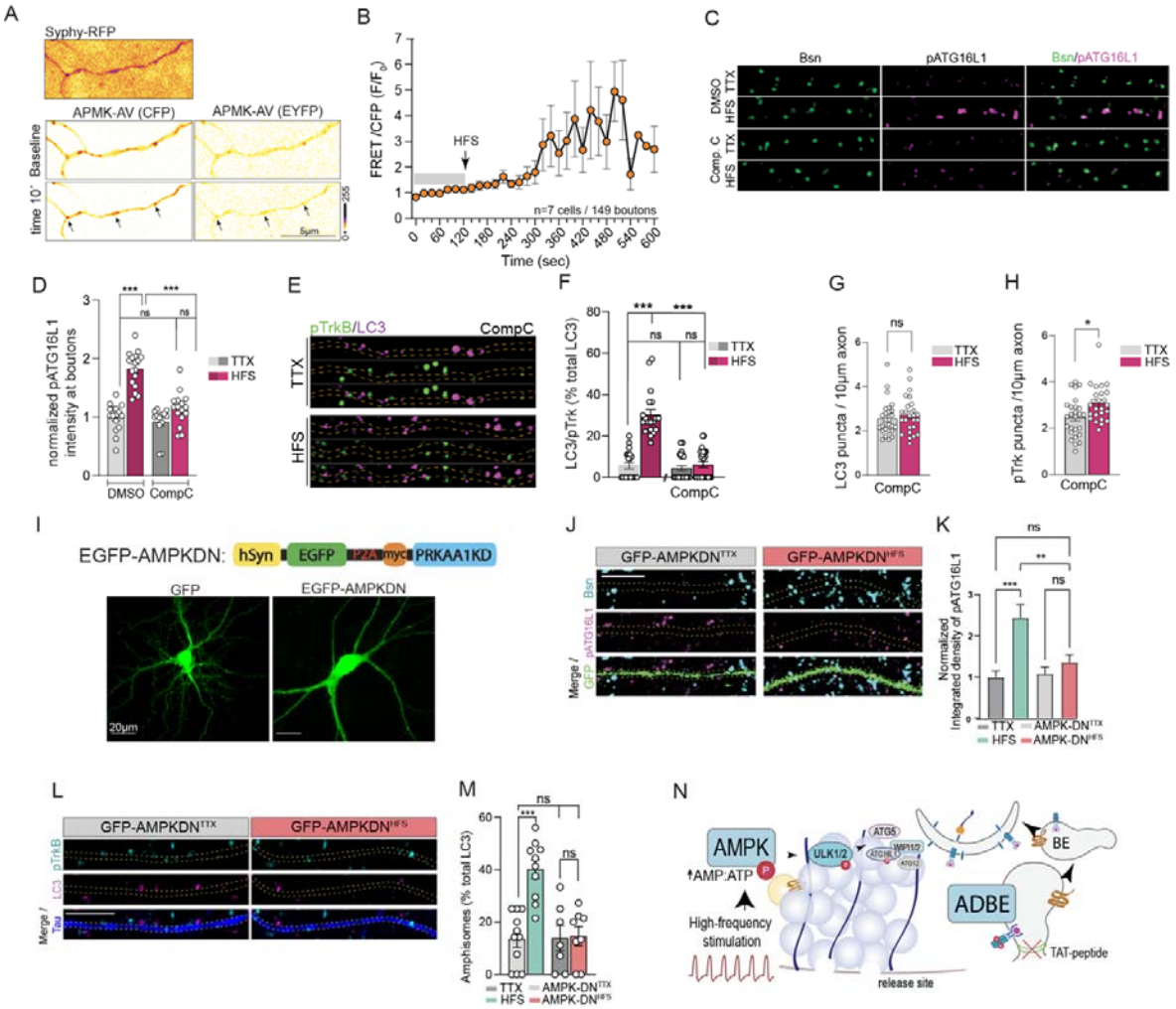


**Figure 5. Synaptic autophagy and amphisome formation occur upon increased energy demands and AMPK activation.**

A) Representative images of primary neurons expressing AMPK-FRET sensor at different time-points over the course of the experiment. Boutons are detected by expression of Sphy-tRFP. Scale bar is 5µm.
B) Quantification of CFP/YFP as indicative of AMPK activation from the experiment in A.
C) Representative images of the primary neurons treated with TTX or HFS in the presence of the AMPK inhibitor Compound C (CompC) or DMSO as control and immunostained with Bassoon and pATG16L1.
D) Quantifying pATG16L1 intensity measured in Bassoon-positive regions from the experiment in C. (n=16 from 2 independent cultures)
E) Representative images of of axons identified by Tau from primary hippocampal neurons treated with CompC or DMSO at DIV14 immunostained against pTrkB and LC3 to detect amphisomes.
F) Quantification of LC3/pTrkB-positive vesicles per 10µm axon from the experiment in E.
G) Quantification of LC3 puncta per 10µm axon from the experiment in G.
H) Quantification of pTrkB puncta per 10µm from the experiment in G.

*(E-H) n=25(HFS+Comp C.); n=26 (TTX+Comp. C) from 3 independent cultures*

I) Scheme showing the expression vector used in AMPK-dominant negative (AMPK-DN) experiments. Expression of GFP and AMPK-DN in the same cells is achieved by means of a P2A sequence. In control experiments an empty GFP construct is used. Representative images of transfected cells are shown below.

J) Representative images of primary neurons expressing a dominant-negative form of AMPK tagged with GFP (GFP-AMPK-DN) and treated with TTX or HFS. After fixation, cells were immunostained for pATG16L1, Tau and Bassoon.

K) Quantification of pATG16L1 intensity at presynaptic boutons labelled by Bassoon from the experiment in K. GFP-expressing cells were used as a control for comparison with the GFP-AMPK-DN group.

L) Representative images of axons expressing GFP-AMPK-DN and immunostained against LC3/pTrkB following TTX or HFS for amphisome quantification.

M) Quantification of amphisomes in GFP-AMPK-DN- positive or GFP-positive (control) axons from the experiment in M.

N) Cartoon depicting the two processes underlying amphisome formation in the presynapse. Activity dependent bulk endocytosis and AMPK activation.

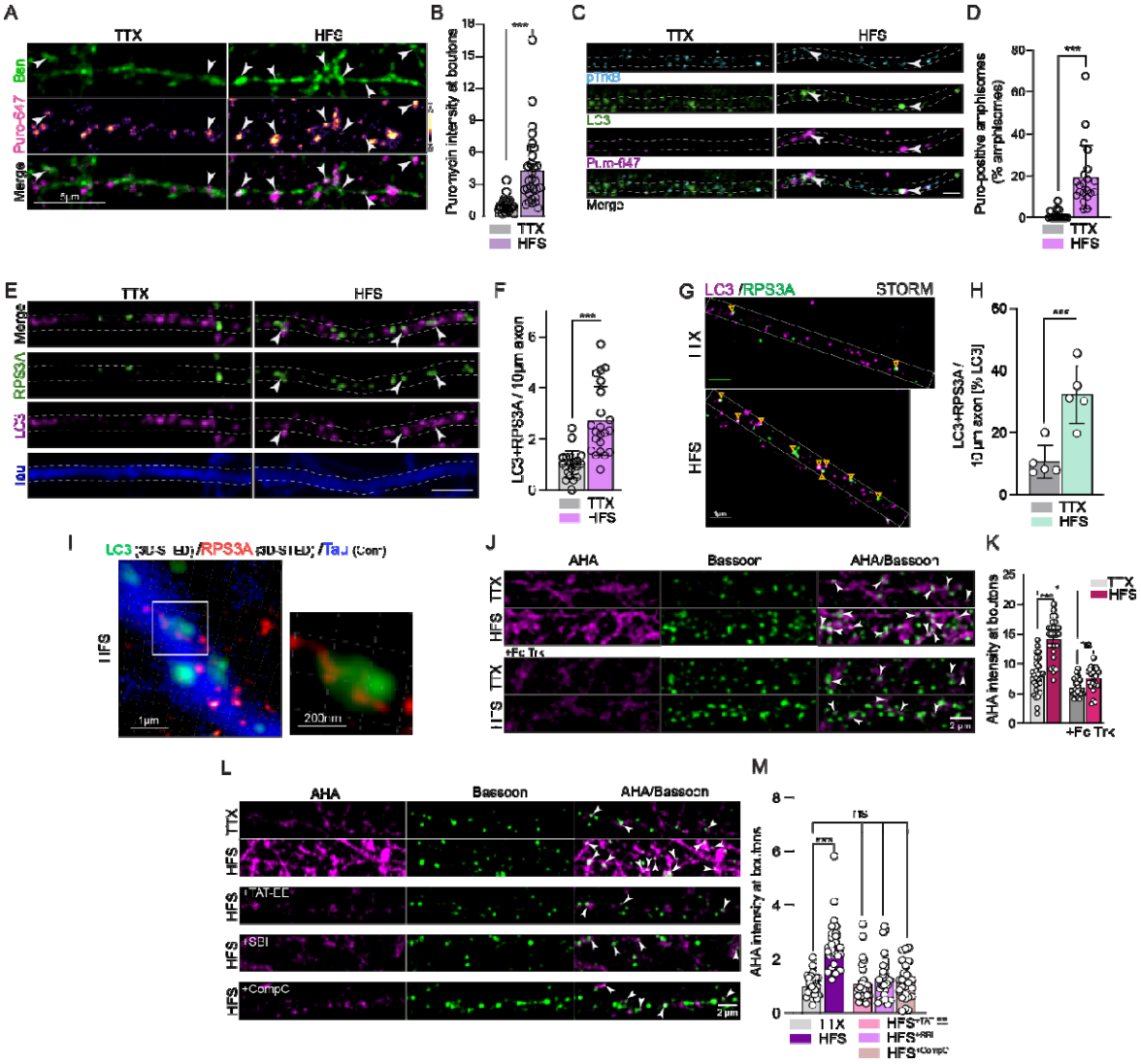


**Figure 6. Amphisome formation is coupled to de-novo protein synthesis**

A) Representative images of neurons treated with TTX or HFS in the presence of Puromycin-647 and immunostained against Bassoon.
B) Bar graph depicting the intensity quantification of puromycin at the presynapse marked with Bassoon mask. *n=30(HFS); n=27 (TTX) from 3 independent cultures*
C) Representative images of neurons treated with TTX or HFS in the presence of Puromycin-647 and immunostained against LC3 and pTrk for amphisome detection.
*D)* Quantification of LC3 and pTrkB puncta positive for puromycin. *(n=21 (HFS); n=22(TTX) from 3 independent cultures*
E) Representative images of neurons immunostained against LC3, RPS3A and Tau and treated with TTX or HFS.
*F)* Quantification of the number of RPS3A-positive LC3 vesicles along axons from neurons treated with TTX or HFS.
*G)* Representative images of axons from neurons treated with TTX or HFS and immunostained against RPS3A, LC3 and Tau. Samples were imaged with

superresolution STORM nanoscopy. Image acquired with Abbelight SAFe MN360 in STORM using Abbelight Smart Kit buffer. Scale bar is 1µm.

*H)* Quantification of the number of RPS3A-positive LC3 vesicles from the experiment in G.

I) 3D-STED nanoscopy showing the close association of of RPS3A to LC3-positive structures in HFS-treated neurons.

*J)* Representative images of presynapses immunostained with Bassoon and newly synthesized proteins labelled with AHA over biotin-click reaction in neurons treated with TTX or HFS in the presence or absence of Fc-Trk bodies that chelate BDNF.

*K)* Quantification of AHA intensity at boutons measured in Bassoon mask, comparing TTX condition to HFS of control and Fc bodies treated neurons from the experiment in K. *n=28 (TTX); n=27 (HFS); n=29(Fc TTX); n=26 (Fc FS) of 3 independent cultures*

*L)* Representative images of presynapses immunostained with Bassoon and newly synthesized proteins labelled with AHA over biotin-click reaction in neurons treated with TTX or HFS in the presence TAT-EE, SBI or CompC.

*M)* Quantification of AHA intensity at boutons measured in Bassoon mask from the experiment in L. *n=29 (TTX); n=28 (HFS); n=27 (TAT); n=28 (SBI), n=27 (Comp.C) of 3 independent cultures*

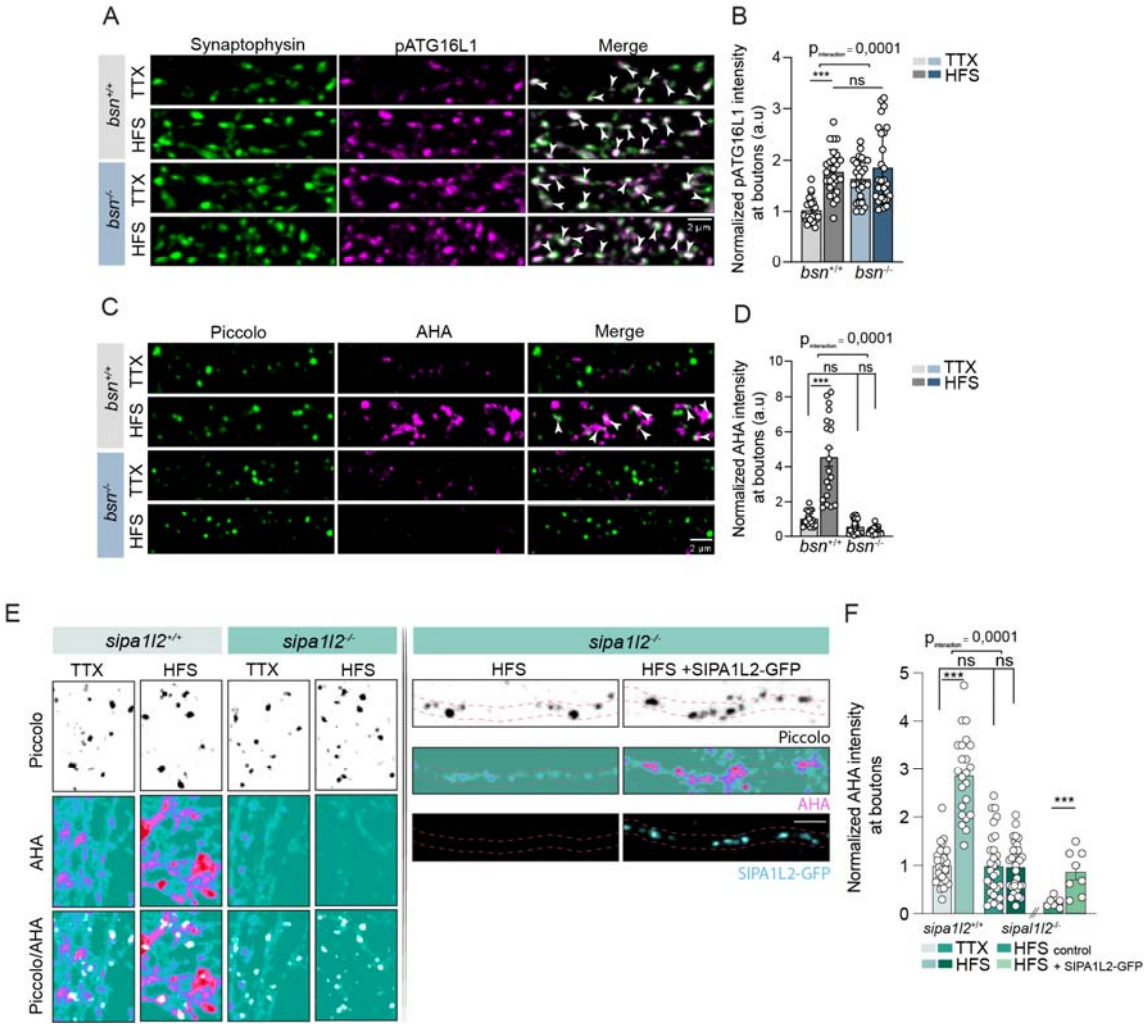


**Figure 7. In *Bsn*- and *SIPA1L2*-deficient neurons activity-dependent amphisome formation is not coupled to local translation**

A) Representative images of *bsn*$^{+/+}$ or *bsn*$^{-/-}$ neurons that underwent treatment with TTX or HFS and immunostaining with Synaptophysin and pATG16L1.

*B)* Quantification of pATG16L1 levels at boutons from the experiment in A. *n=24-27 from 3 independent cultures*

C) Images represent presynapses immunostained with Piccolo and newly synthesized proteins labelled with AHA over biotin-click reaction from *bsn*$^{+/+}$ or *bsn*$^{-/-}$ treated with TTX or HFS.

D) Quantification of AHA intensity at boutons measured in Piccolo mask, comparing TTX condition to high frequency stimulation of WT to KO mice. Bar graph to E. *n=20 from 2 independent cultures*

E) Images represent presynapses immunostained with Piccolo and newly synthesized proteins labelled with AHA over biotin-click reaction from *sipa1l2*$^{+/+}$ or *sipa1l2*$^{-/-}$ treated with TTX or HFS. Additionally SIPA1L2-GFP was overexpressed in knockout animals in stimulated cells, using non-transfected cells as control.

F) Quantification of AHA intensity at boutons measured in Piccolo mask, comparing TTX condition to high frequency stimulation of *sipa1l2*$^{+/+}$ or *sipa1l2*$^{-}$

$^{/-}$ mice. Showing aswell quantification of AHA intensity in SIPA1L2-GFP overexpressing cells to stimulated control in *sipa1l2*$^{-/-}$ mice. Bar graph to E.

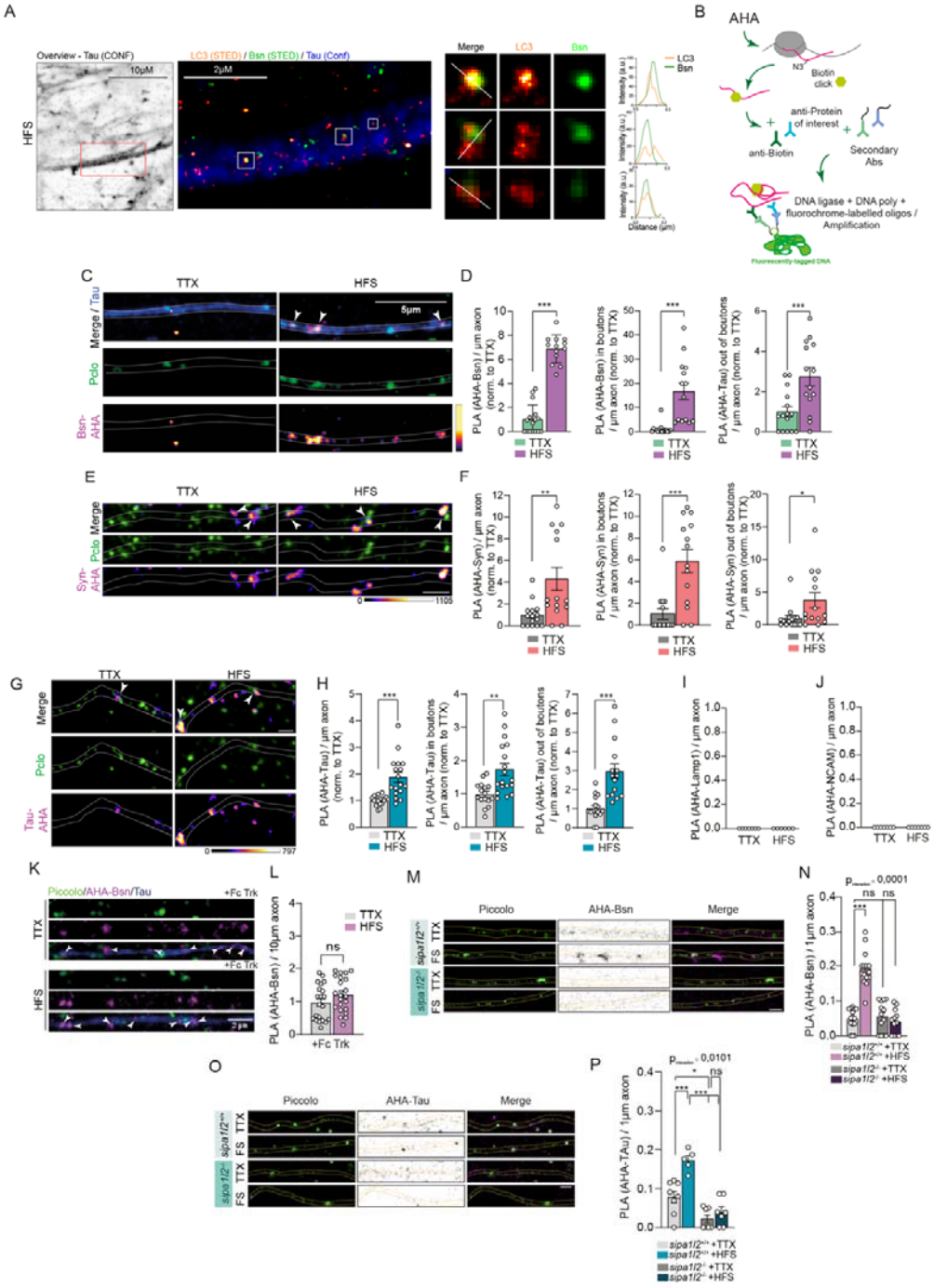


**Figure 8. BDNF-TrkB amphisomes drive the degradation of key presynaptic proteins and the local translation of their mRNA**

A) 3D-STED nanoscopy shows the close association and similar distribution of Bassoon and LC3 along axons detected with Tau (confocal).

B) Schematic representation depicting the principle of FUNCAT-PLA used in the experiments from C to P.
C) Representative confocal images of axons showing local translation of Bassoon by means of FUNCTA-PLA following HFS as compared to TTX-treated cells. Scale bar, 5 µm. White arrows indicate newly synthesized protein of interest.
D) Quantification of PLA signal of locally synthesized Bassson in axons from the experiment in C. Quantification of PLA signal in and outside of boutons labelled with Piccolo in axons.
E) Representative confocal images of axons showing local translation of Synapsin by means of FUNCTA-PLA following HFS as compared to TTX-treated cells. Scale bar, 2 µm. White arrows indicate newly synthesized protein of interest.
F) Quantification of PLA signal of locally synthesized Synapsin in axons from the experiment in E. Quantification of PLA signal in and outside of boutons labelled with Piccolo in axons.
G) Representative confocal images of axons showing local translation of Synapsin by means of FUNCTA-PLA following HFS as compared to TTX-treated cells. Scale bar, 2 µm. White arrows indicate newly synthesized protein of interest.
H) Quantification of PLA signal of locally synthesized Synapsin in axons from the experiment in G. Quantification of PLA signal in and outside of boutons labelled with Piccolo in axons.
I,J) Quantification of PLA signal of locally synthesized LAMP1 (I) or NCAM (J).
K) Representative confocal images and quantification of newly synthesized Bassoon at the presynapse labelled with piccolo in DIV14-16 cultured hippocampal neurons treated with Fc Trk bodies overnight.
L) Quantificaiton of the local translation of Bassoon upon HFS with Fc Trk bodies from the experiment in K.
M-P) PLA signal of Bassoon (M,N) and Tau (O,P) of DIV18 cultured hippocampal neurons in Sipa1L2 WT and KO mice treated with TTX or HFS. *Sipa1l2*$^{-/-}$ neurons show no elevated PLA signal after HFS for newly synthetized Bassoon and Tau. (N) n = 17–19 cells from 2 independent cultures, (P) n= 5-8 from 1 culture.
Data are plotted as average ± SEM.

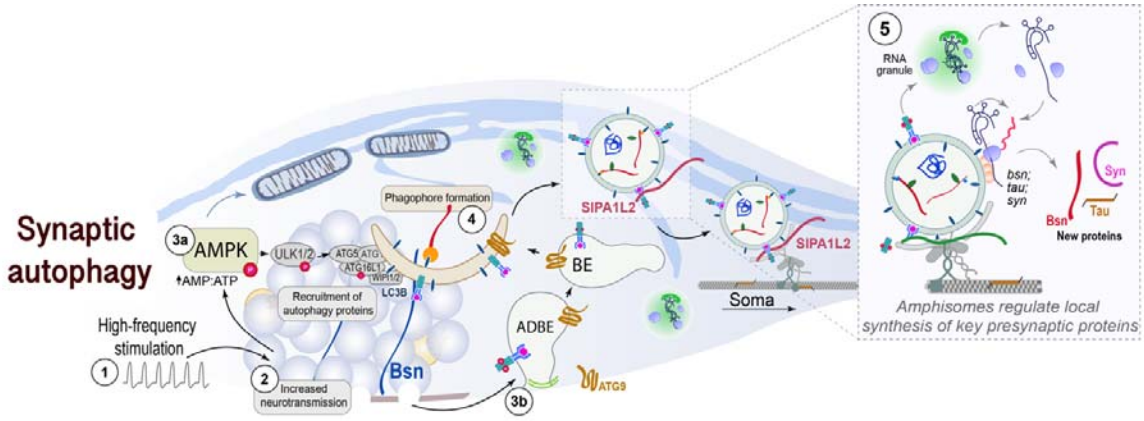


**Figure S5: Underlying mechanism of amphisome formation at boutons**
Under basal conditions smooth endoplasmic reticulum in axons and boutons is the most prominent site of continuous autophagosome formation. Following HFS (1), intense SV recycling (2) causes an increase in the AMP:ATP ratio that leads to the activation of AMPK (3b) and a recruitment of autophagy proteins to the bouton. AMPK triggers autophagy initiation at boutons. Concomitantly bulk-endocytosis takes place following HFS (3b) and the formation of a bulk endosome (BE) supports amphisome formation (4). BDNF/TrkB signaling from signaling amphisomes initiates the local synthesis of presynaptic proteins (5) essential for the maintenance and stability of presynaptic biomolecular condensates (bsn, tau, syn) which, in turn, are likely to serve as cargo in amphisomes. In this way, signaling amphisomes enable the local replacement of essential presynaptic proteins.